Reviews and syntheses: Expanding the global coverage of gross primary production and net community production measurements using BGC-Argo floats

Robert W. Izett[1], Katja Fennel[1], Adam C. Stoer[1], David. P. Nicholson[2]

[1]Department of Oceanography, Dalhousie University, Halifax, B3H 4R2, Canada
[2]Marine Chemistry and Geochemistry Department, Woods Hole Oceanographic Institution, Woods Hole, 02543, USA

Correspondence to: Robert Izett (robert_izett@live.com); Katja Fennel (Katja.Fennel@Dal.Ca)

Abstract. This paper provides an overview and demonstration of emerging float-based methods for quantifying gross primary production (GPP) and net community production (NCP) using Biogeochemical-Argo (BGC-Argo) float data. Recent publications have described GPP methods that are based on the detection of diurnal oscillations in upper ocean oxygen or particulate organic carbon concentrations using single profilers or a composite of BGC-Argo floats. NCP methods rely on budget calculations to partition observed tracer variations into physical or biological processes occurring over timescales greater than one day. Presently, multi-year NCP time-series are feasible at near-weekly resolution, using consecutive or simultaneous float deployments at local scales. Results, however, are sensitive to the choice of tracer used in the budget calculations and uncertainties in the budget parametrizations employed across different NCP approaches. Decadal, basin-wide GPP calculations are currently achievable using data compiled from the entire BGC-Argo array, but finer spatial and temporal resolution requires more float deployments to construct diurnal tracer curves. A projected, global BGC-Argo array of 1000 floats should be sufficient to attain annual GPP estimates at 10-degree latitudinal resolution, if floats profile at off-integer intervals (e.g., 5.2 or 10.2 days). Addressing the current limitations of float-based methods should enable enhanced spatial and temporal coverage of marine GPP and NCP measurements, facilitating global-scale determinations of the carbon export potential, training of satellite primary production algorithms, and evaluations of biogeochemical numerical models.

1 Introduction

Marine primary production (PP), the photosynthetic production of organic carbon and oxygen (O_2), is a foundational process for ocean ecosystems. PP sustains marine life, strongly correlates with fisheries yields (e.g., Ware and Thomson, 2005), and influences the planet's climate by contributing to atmospheric carbon dioxide (CO_2) sequestration via the biological carbon pump (Volk and Hoffert, 1985; Siegenthaler and Sarmiento, 1993). Climate change is expected to have a heterogeneous, albeit uncertain, effect on the timing, magnitude, and variability of PP across the global ocean (e.g., Polovina et al., 2008; Bopp et al., 2013; Westberry et al., 2012), with potentially significant impacts on marine food webs and the biological carbon sink (e.g., Hoegh-Guldberg and Bruno, 2010; Ainsworth et al., 2011). To understand and predict these climate-dependent changes

30 with confidence, it is crucial to monitor PP variability on ecologically relevant space and time scales. Autonomous profiling instruments, such as biogeochemical Argo (BGC-Argo) floats, offer great potential to achieve this objective by augmenting traditional PP sampling approaches and enhancing the spatial (horizontal and vertical) and temporal coverage of PP estimates (Chai et al., 2020).

At the ecosystem level, PP can be quantified by the following common metrics: gross primary production (GPP), net primary

35 production (NPP), and net community production (NCP) (Fig. 1). GPP measures community-wide photosynthesis, representing the total production of organic carbon or O_2 by autotrophs (e.g., phytoplankton, cyanobacteria) and represents the photosynthetic energy availability to the entire food web. GPP is reported as gross oxygen production (GOP) or gross carbon production (GCP), when defined in O_2 or carbon equivalents, respectively. NPP refers to the net production of autotroph biomass when accounting for autotrophic respiration (i.e., organic matter oxidation; AR), and represents the amount of

40 photosynthetically produced organic carbon available to heterotrophs (e.g., bacteria, zooplankton, fish). Lastly, NCP is the difference between GPP and respiration by autotrophs and heterotrophs (i.e., community respiration, CR), and therefore determines if an ocean region is net autotrophic (net production, indicated by NCP > 0) or net heterotrophic (net consumption and NCP < 0). When measured over sufficiently large temporal and spatial scales, NCP quantifies the amount of photosynthetically produced organic matter that sinks from the upper ocean (Laws 1991). All PP fractions are often expressed

45 as volumetric equivalents of organic carbon or O_2 production (e.g., mol C or O_2 m^{-3} d^{-1}), such that respiration has negative values.

A variety of approaches and sampling platforms have been used to quantify PP. The earliest method estimates NCP and CR (and thus GOP) by measuring the evolution of O_2 in natural seawater samples incubated in light and dark bottles, respectively (Gaarder and Gran, 1927). Other incubation-based approaches involve spiking samples with [14]C- or ^{13}C-labelled bicarbonate

50 (GPP and NPP; Steeman Nielsen, 1952; Slawyk et al., 1977) or ^{18}O-labelled water (GOP; Bender et al., 1987; Ferrón et al., 2016) to trace temporal changes in photosynthetic biomass or O_2 production under realistic incubation conditions. These incubation approaches, though, are subject to various experimental biases, including containment effects on the plankton community, sensitivity to the incubation duration, and the excretion of labelled dissolved organic carbon (e.g., Pei and Laws, 2013; Cullen, 2001). The O_2-to-argon (O_2/Ar; Reuer et al., 2007; Spitzer and Jenkins, 1989) and triple O_2 isotope (Luz and

55 Barkan, 2000) methods thus emerged as tracer-based techniques for measuring PP from in situ observations and biogeochemical budget calculations. While the original incubation and tracer-based approaches have been applied widely, they require the collection of discrete samples from ships and therefore yield limited data coverage. Fortunately, advances in instrumentation have facilitated underway measurements of O_2/Ar and particulates at the surface, giving rise to methods for high-resolution ship surveys of NCP and NPP, respectively (Tortell, 2005; Kaiser et al., 2005; Burt et al., 2018). Sampling via

60 instrumented moorings similarly enabled high temporal resolution GPP and NCP time-series at fixed positions (e.g., Emerson and Stump, 2010; Johnson, 2010; Weeding and Trull, 2014; Fassbender et al., 2016). Yet, while promising, these ship and mooring-based approaches are subject to trade-offs between temporal, horizontal, and vertical measurement resolution. Moreover, many traditional approaches require expensive instrumentation (underway approaches) or considerable human

oversight to collect the necessary data (incubation approaches), making them broadly inaccessible to the oceanography

65 community or impractical for autonomous surveys. As a result of the challenges associated with the traditional PP methods, there are substantial gaps in PP datasets, with many ocean regions being under-sampled or omitted from archived records (Fig. 2a,b). While satellite and statistical algorithms can provide PP estimates (Behrenfeld and Falkowski, 1997; Huang et al., 2021; Li and Cassar, 2016) with enhanced space-time coverage, their utility is constrained by limitations such as the accuracy of satellite ocean colour observations (e.g., Long et al., 2021) and the inability to strongly detect subsurface information (Gordon

70 and McCluney, 1975) where PP may still be significant.
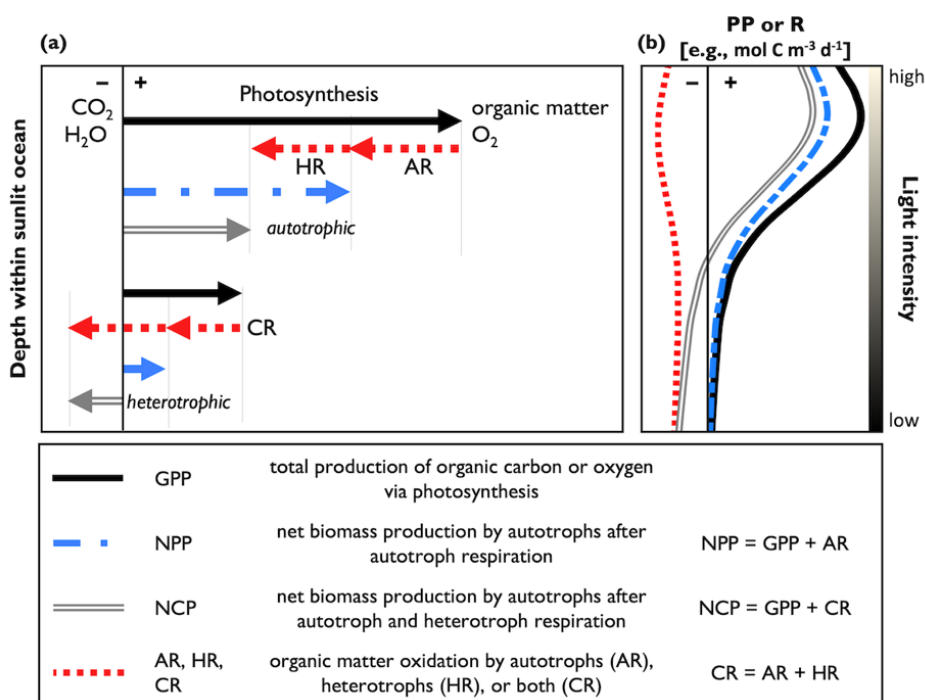
Figure 1. A conceptual schematic of PP definitions. Panel (a) shows a simplified reaction equation of organic matter production and respiration in representative autotrophic (NCP > 0) and heterotrophic (NCP < 0) sections of the sunlit ocean. Panel (b) represents
75 **idealized PP and CR profiles, where PP declines with depth due to the light dependency of photosynthesis. The vertical axis represents water column depth, and the thin black line divides positive and negative rates.**

Considering the challenges associated with the above-mentioned traditional PP approaches, emerging methods that use autonomous profiler observations present a significant opportunity to expand the spatial and temporal coverage of PP datasets

80 and improve satellite-based observations via hybrid approaches. The BGC-Argo program, in particular, supports a growing array of profiling floats that provide continuous biogeochemical observations (e.g., O_2, pH, nitrate, chlorophyll fluorescence, particle backscatter as a proxy for organic matter) in the upper 2000 m of the global ocean at ~5- or 10-day intervals (Fig. 2d). The BGC-Argo fleet has grown steadily in recent years (>500 operational floats as of Feb. 2023), and the international

community is targeting a sustained deployment of 1000 BGC floats distributed equally throughout the global ocean (Roemmich

85 et al., 2021; Biogeochemical-Argo Planning Group., 2016). Several recent studies have quantified PP using BGC-Argo floats
and other autonomous profilers, including gliders (see Table A1 in the appendix, and references therein), demonstrating the
potential to derive year-round, depth-resolved PP estimates in remote ocean regions (Fig. 2c).

The primary objective of this paper is to demonstrate the potential of autonomous platforms, exemplified by BGC-Argo floats,
for expanding the spatial and temporal coverage of PP estimates. In particular, this paper explores float-based approaches for

90 estimating GPP and NCP, since those methods are more mature than emerging approaches for NPP quantification. To facilitate
a full exploitation of these new opportunities, we take stock of the float-based tools currently available to researchers and
identify their strengths and limitations. After providing an overview of the emerging float- and glider-based PP approaches,
we present quantitative analyses to demonstrate the current application of these methods.
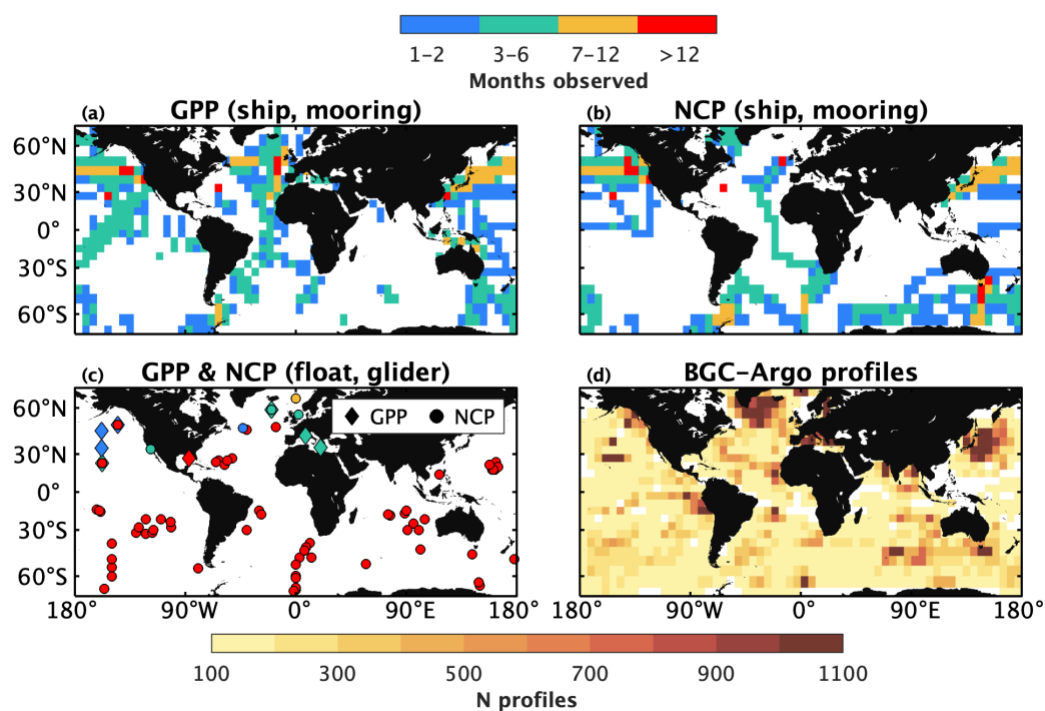
95

Figure 2. Coverage of GPP and NCP datasets, and BGC-Argo profiles. The upper row represents archived GPP and NCP data obtained from ships or moorings, while panel (c) shows the locations and durations of float- or glider-based GPP and NCP studies. Panel (d) shows a heatmap of the locations of BGC-Argo profiles collected from 2010 through 2022. Data in panels (a), (b) and (d) are binned into a five-by-five-degree grid. A list of archived data sources is provided in the appendix.

2 Overview of approaches and application details

This section provides an overview of approaches to quantifying GPP (measured as GOP and GCP) and NCP using observations made by BGC-Argo and other autonomous profilers. For each approach, we outline the premise and describe the specific variables used, sampling requirements, assumptions, and variations.

To date, autonomous GPP approaches have relied on measurements of O_2 and particulate organic carbon (POC). NCP calculations have relied on O_2, POC and nitrate (NO_3^-) measurements and estimates of dissolved inorganic carbon (DIC) and total alkalinity (TA). These tracers are selected because their concentrations in the sunlit ocean are impacted by primary production (photosynthesis and respiration). Other sources and sinks, such as exchange across the air-sea interface, vertical mixing, advection, and/or sinking and grazing, also impact the concentrations of these tracers. Accordingly, the temporal change in the concentration of a tracer, T, can be represented by the following general budget equation

$$\underbrace{d[T(t,z)]/_{dt}}_{measured} = \underbrace{GPP(t,z) + CR(t,z) + \text{other sources/sinks}(t,z)}_{estimated} \tag{1}$$

where $[T(t,z)]$ is the measured tracer concentration at time, t, and depth, z, and $d[T(t,z)]/_{dt}$ is its time rate of change, expressed in concentration units per unit time (e.g., mmol C m^{-3} d^{-1}). Autonomous GPP methods interpret Eq. 1 over a 24-hr period and are premised on the widespread observation of diurnal cycles in O_2 and POC concentrations (Fig. 3). These cycles result from the dependency of photosynthesis on sunlight and are driven by daytime net autotrophic production (GPP + CR) and nighttime CR (e.g., Siegel et al., 1989; Johnson et al., 2006). Assuming that diurnal variability in the other source/sink terms in Eq. 1 is negligible, and that CR is constant over a 24-hr period, Eq. 1 can be approximated by the following equation

$$d[T(t,z)]/_{dt} \approx GPP(t,z) + CR(z) \tag{2}$$

where T is O_2 or POC. Given Eq. 2, vertically resolved GCP or GOP estimates can be derived if the diurnal cycles of POC or O_2 in the euphotic zone are detectable.

Autonomous NCP approaches, in contrast, seek to interpret temporal changes in the concentration of a photosynthesis-respiration tracer over timescales exceeding one day (typically on the order of one week or more). Over these timescales, variability in the non-photosynthesis/respiration terms in Eq. 1 is not negligible. NCP (i.e., GPP+CR) is thus determined by re-arranging Eq. 1, as follows, and estimating the contributions of the other source/sink terms to the observed tracer time-series,

$$NCP(t,z) = d[T(t,z)]/_{dt} - \text{other sources/sinks}(t,z). \tag{3}$$

Eq. 3 is typically evaluated at discrete time and depth intervals equivalent to the resolution of profiling measurements, or by integrating quantities over coarser depth ranges, e.g., the mixed layer.

135 As GPP and NCP methods evaluate Eq. 1 over contrasting timescales, different sampling approaches have been employed to obtain the requisite tracer time-series observations. For GPP calculations, multiple measurements per day are necessary to adequately resolve the diurnal cycle. Initially, GPP studies used a single profiling instrument, such as a glider (Nicholson et al., 2015; Barone et al., 2019), Lagrangian surface float (Briggs et al., 2018), or biogeochemical profiling float whose mission cycle was adjusted for frequent upper ocean profiling (Barbieux et al., 2022; Gordon et al., 2020; Henderikx Freitas et al.,

140 2020) (Fig. 3a,b). Gordon et al. (2020) and Barbieux et al. (2022), for example, used floats with profiling intervals of 3 and 6 hrs, respectively, to obtain diurnal cycle observations. The majority of the BGC-Argo fleet, however, collects a water column profile every ~5 or 10 days. As a result, a diurnal cycle cannot be resolved using data from a single BGC-Argo float profiling at these intervals. This limitation was resolved by Johnson and Bif (2021) and Stoer and Fennel (2022) who quantified GOP and GCP from daily O_2 or POC cycles using a composite of observations from multiple floats within selected geographic

145 regions. To achieve roughly equal coverage of all hours of the day, they compiled data from floats that profiled at non-integer intervals (e.g., 10.2, not 10.0 days). Then, GPP was estimated by fitting the photosynthesis curve through all the resulting data points (as in Johnson and Bif, 2021), or by first calculating hourly median POC or O_2 values (Stoer and Fennel, 2022) (Fig. 3c). Importantly, data from floats that do not sample all hours of the day evenly must be removed so that the resulting GPP estimates are not biased to a specific time of day. A non-integer sampling interval of 5.2 or 10.2 has been recommended to

150 achieve approximately equal coverage of all hours over a float's lifecycle (Johnson and Bif, 2021; Stoer and Fennel, 2022). While GOP or GCP estimates derived from rapid profiling may yield daily temporal resolution (i.e., one GPP estimate per daily cycle) in ocean regions with strong diurnal variations, estimates derived from composite curves are more representative of typical conditions over the time and space scales that the data are composited. Sampling for NCP determinations has most commonly been based on nominal BGC-Argo profiling intervals, although high-resolution sampling using rapidly profiling

155 floats is also feasible. Resulting NCP estimates have optimal vertical and temporal resolutions equivalent to those of the sampling profiling observations.

To estimate GOP, O_2 is best expressed as a concentration anomaly, ΔO_2, calculated as the difference between observed and equilibrium concentrations (i.e., $\Delta O_2 = O_2 - O_{2,equil}$; all typically mmol O_2 m^{-3}). Equilibrium concentrations are calculated using corresponding temperature and salinity observations (Garcia and Gordon, 1992). This practice is recommended to minimize

160 potential diurnal solubility effects on $d[O_2(t,z)]/dt$. In NCP calculations, O_2 is expressed as its absolute concentration. POC concentrations (typically mg m^{-3}) for GCP and NCP calculations are derived from particle backscatter (b_{bp}) or beam attenuation (c_p, typically at 660 nm) measurements (both m^{-1}) using regional (e.g., Loisel et al., 2011; Cetinić et al., 2012) or global (e.g., Graff et al., 2015) algorithms. Many algorithms estimate POC from b_{bp} at 700 nm ($b_{bp,700}$), the wavelength that is most commonly measured by BGC-Argo floats. For algorithms that rely on different b_{bp} wavelengths (e.g., b_{bp} at 470 nm, as in the

165   algorithm of Graff et al., 2015), a power-law equation is required to convert between $b_{bp,700}$ and b_{bp} at other wavelengths (Boss et al., 2013; Boss and Haëntjens, 2016). Only a subset of floats directly measures $b_{bp,470}$ or $c_{p,660}$. Lastly, NCP estimates derived from TA and DIC budgets rely on float pH measurements and an empirical TA function (Huang et al., 2022), where TA is estimated from float O_2 and hydrographic observations using a neural network algorithm (e.g., Bittig et al., 2018; Carter et al., 2021). DIC is subsequently calculated from pH and TA based on known seawater carbonate system relationships (Gattuso et

170   al., 2022).

2.1 GPP

Given a diurnal POC or O_2 time-series, GCP or GOP have been estimated using three different mathematical algorithms that describe the shape of the diurnal curve. Two of the approaches have been applied only using single profilers making multiple

175   measurements of the upper ocean each day; the other has been adapted for composite daily cycles (Fig. 3). Each method yields one daily GPP estimate per diurnal curve, and estimates may be vertically resolved or integrated, depending on the sampling infrastructure used. As a result, the spatial and temporal resolution of the following methods is constrained by the measurement resolution of the float or glider.

Briggs et al. (2018) described a method that requires estimating tracer sink terms (including CR) by fitting a type I linear

180   regression to nighttime (sunset to sunrise) POC or O_2 data (red line in Fig. 3a). Extrapolating the regression line from the POC or O_2 value at sunrise (sunset) to noon on the following (preceding) day (dashed line in Fig. 3a) then yields an estimate of the tracer's mid-day concentration in the absence of photosynthesis. The difference between observed noontime concentrations ($[T(t,z)]_{observed}$) and the value predicted by the regression extrapolation ($[T(t,z)]_{predicted}$) is an indication of GPP, so that GPP is calculated as follows

185

$$GPP(z) = ([T(z)]_{predicted} - [T(z)]_{observed})\,(0.5\ \text{day}^{-1}). \tag{4}$$

Daily GPP is taken as the average of morning and afternoon values. This method has been applied by constructing diurnal O_2 or c_p-POC cycles from continuous, upper ocean observations using a Lagrangian surface float (Briggs et al., 2018), or from a

190   float profiling at 3-hr intervals (Gordon et al., 2020). In both cases, surface layer-integrated GPP estimates were obtained by integrating O_2 or POC observations within a density-defined layer. A minimum upper ocean sampling resolution of ~3-4 hr is likely necessary to obtain a robust nighttime regression fit to the data and to derive GPP at daily resolution.

Barbieux et al. (2022), following Claustre et al. (2008), introduced another approach for GCP derivations from a rapidly-profiling BGC-Argo float deployed in the Mediterranean Sea. In their method, GCP is estimated by solving the following

195   differential equation for the time rate of change in depth-resolved POC concentrations

$$d[POC(t,z)]\big/_{dt} = \mu(t,z)\, POC(t,z) - L(t,z)\, POC(t,z), \tag{5.1}$$

where μ represents autotrophic growth, and L represents particle losses due to CR, sinking, and grazing (both d^{-1}). Eq. 5.1 is a

200 variation of Eq. 2, where $\mu(t,z)\, POC(t,z)$ and $L(t,z)\, POC(t,z)$ are equivalent to $GPP(t,z)$ and $CR(t,z)$, respectively. Integrating Eq. 5.1 between sunset (SS_0) and the following sunrise (SR_1), when $\mu=0$, yields an estimate for the loss term,

$$L(z) = \frac{\ln\left(POC(z,SS_0)\big/POC(z,SR_1)\right)}{SR_1 - SS_0}. \tag{5.2}$$

205 Combining Eqs. 5.1 and 5.2, assuming constant L(z), and integrating over a full day (sunrise to sunrise; SS_0 to SS_1) produces the following equation for daily GPP

$$GPP(z) = POC(SR_1,z) - POC(SR_0,z) + L(z) \sum_{i=1}^{j}(t_{i+1} - t_i)\frac{POC(t_{i+1},z) + POC(t_i,z)}{2}, \tag{5.3}$$

210 where the index i represents time-resolved POC measurements from sunrise on the first day (SR_0) to sunrise on the following day (SR_1) (Fig. 3b). Barbieux et al. (2022) used a BGC-Argo float profiling at 6-hr intervals, thus enabling GCP calculations with daily resolution. POC quantities were integrated vertically in three upper ocean layers.

A third approach for estimating GPP has been applied successfully using O_2 observations from gliders (Nicholson et al., 2015; Barone et al., 2019), a rapidly profiling BGC-Argo float (Henderikx Freitas et al., 2020), and a composite of O_2 and b_{bp}-POC

215 cycles from BGC-Argo floats (Johnson and Bif, 2021; Stoer and Fennel, 2022). In this method, introduced by Nicholson et al. (2015), Eq. 2 is re-written to describe discrete, time-dependent changes in POC or O_2 as a function of time-variable irradiance, E(t),

$$T(t_1,z) = T(t_0,z) + GPP(z)\frac{\int_{t_0}^{t_1} E(t)dt}{\bar{E}} + CR(z)(t_1-t_0), \tag{6}$$

220

given $d[T(t,z)]\big/_{dt} \approx \frac{[T(t_1,z)] - [T(t_0,z)]}{t_1-t_0}$, and where $\bar{E}$ and t_1-t_0 are the mean daily irradiance level and time step, respectively. The

middle term, $GPP(z)\frac{\int_{t_0}^{t_1} E(t)dt}{\bar{E}}$, represents photosynthesis as a function of time-varying irradiance, which is calculated from

geospatial (location and time) data. A photosynthesis-versus-irradiance (P-vs-E), a sinusoidal, and a linear algorithm have

been proposed for $\frac{\int_{t_0}^{t_1} E(t)dt}{\bar{E}}$ (see coloured lines in Fig. 3c), although resulting GPP estimates are not statistically different across

225 models (Barone et al., 2019; Henderikx Freitas et al., 2020). Given time-resolved ΔO_2 or POC observations, Eq. 6 can be re-

expressed as a system of linear equations (see Eq. 4 in Barone et al., 2019), and GPP and CR are approximated as the least squares coefficients required to fit $\frac{\int_{t_0}^{t_1} E(t)dt}{\bar{E}}$ to the observed diurnal cycle. MATLAB code for solving the system of linear equations has been provided by Barone et al. (2019) and modified by Johnson and Bif (2021). Stoer and Fennel (2022) modified the code further and adapted it for Python.

230 To simplify the system of equations, Nicholson et al. (2015), Johnson and Bif (2021) and Stoer and Fennel (2022) assumed equivalency between daily integrated GPP and CR. Although the assumption is physically invalid in many ocean regions since it may unrealistically constrain daily NCP to zero, it enables calculations of statistically robust GPP estimates in ocean regions where diurnal oscillations are small. Barone et al. (2019), in contrast, calculated separate GPP and CR values, albeit with larger errors in each term. Similarly, Gordon et al. (2020) attempted separate GPP, CR, and NCP estimates by applying the Briggs

235 et al. (2018) method for float data collected from the Gulf of Mexico.

Surface layer-integrated GOP has been derived by applying this approach to observations obtained from gliders (Nicholson et al., 2015; Barone et al., 2019) or rapidly profiling floats (Henderikx Freitas et al., 2020). In principle, these sampling methods can yield daily diurnal curves and GOP estimates. In practice, however, the resulting GOP values may have an effective temporal resolution of ~5-7 days in low-productivity regions, due, in part, to limited detection (i.e., low signal-to-noise ratio)

240 of daily O_2 oscillations (Barone et al., 2019). Johnson and Bif (2021) and Stoer and Fennel (2022) extended the present approach for composite sampling exploiting the broader BGC-Argo array. Johnson and Bif (2021) collated float ΔO_2 data in different geographic regions between 2010 and 2020, constructing vertically resolved diurnal cycles by binning the composited datasets in 10-m intervals, and averaging values to the nearest local hour. GPP is calculated for a single composited diurnal curve, as described above. Stoer and Fennel (2022) further extended the approach by calculating GCP from b_{bp}-POC and using

245 observations median-binned to each local hour. Using data from a meta-analysis by Moran et al. (2022), they calculated an average percent extracellular release (PER) to account for dissolved organic carbon (DOC) production not detected by the b_{bp} sensor. Accordingly, they scaled their GCP values using the calculated PER value and converted between GCP and GOP using a photosynthetic quotient (PQ) value of 1.4, i.e., GOP $= \frac{GCP}{(1-PER)}$ PQ. Finally, Johnson and Bif (2021) and Stoer and Fennel (2022) derived NPP from the diurnal GPP calculations by applying a global empirical GOP:NPP ratio of 2.7 mol O_2 (mol C)[-]

250 [1] (i.e., NPP = GOP / 2.7).

The horizontal and temporal resolution of the present approach based on composited sampling is limited by the number of floats and profiles in a given geographic region. There must be enough profiles taken equally throughout the day to distinguish a daily signal. Johnson and Bif (2021) estimated that a minimum of 20 and 50 O_2 profiles in each hour (equivalent to 480 to 1200 profiles, per day) are required to clearly detect diurnal variability in tropical and high-latitude waters, respectively. For

255 the region 30–70°S, Stoer and Fennel (2022) estimated that at least 2000 b_{bp} and 5000 O_2 profiles, per diurnal curve, are required to limit the noise-to-signal ratio of the resulting PP estimates to one, or less.

	(a)	(b)	(c)
Sampling Platform	Single profiler, multiple profiles per day	Single profiler, multiple profiles per day	Single profiler, rapidly profiling; multiple floats, profiling at ~5.2- or 10.2-d intervals
Variables used to-date	O_2, b_{bp}-POC, c_p-POC	b_{bp}-POC, c_p-POC	O_2, b_{bp}-POC
Fit approach (Equation)	Difference between observed noontime O_2 or POC and linear regression extrapolation of nighttime data (Eq. 4)	Partial differential equation solved between SS_0 and SR_1 (CR), and between SR_0 and SR_1 (GPP + CR) (Eq. 5)	GPP vs light model (P-vs-E, sinusoidal or linear) fit to diurnal curve (Eq. 6)
Assumptions	*All approaches:* night $\left.\frac{d[T(z)]}{dt}\right| = CR$; day $\left.\frac{d[T(z)]}{dt}\right| = GPP + CR$; CR constant over 24-hr		$GPP = CR^{(1)}$; $\frac{GOP}{GPP} = \frac{PQ}{(1-PER)}{}^{(2)}$
References	Briggs et al., 2018; Gordon et al., 2020	Barbieux et al., 2022	Nicholson et al., 2015; Barone et al., 2019; Henderikx Freitas et al., 2020; Johnson and Bif, 2020; Stoer and Fennel, 2022

260 **Figure 3. Conceptual schematic of autonomous GPP methods. The black markers in the figures represent ΔO₂ or POC observations. In (a) and (b) markers represent data obtained using a single profiling platform, while those in (c) represent median (± standard deviation) data values during each hour of the day. The grey bars represent approximate nighttime periods between sunset (SS) and sunrise the following day (SR). The lower part of the schematic summarizes the approach requirements. The "Variables used to-date" row identifies the tracers that have been used successfully, so far, under each method applied using autonomous profilers. It does not necessarily limit the respective float-based methods to those tracers, alone. Notes: (1) assumption applied in Nicholson et al. (2015), Johnson and Bif (2021), Stoer and Fennel (2022); (2) assumption applied in Stoer and Fennel (2022) only.**

2.2 NCP

265 Autonomous NCP methods invoke a different set of calculations and assumptions than GPP methods. Namely, the sum of non-biological terms (i.e., physical fluxes) is estimated and subtracted from observed tracer changes in discrete time and depth intervals (as in Eq. 3). Equation 3 is commonly solved using a one- or two-dimensional box model approach by partitioning the water column into layers (e.g., mixed layer, euphotic zone) or by discretizing in depth intervals (Table 1; Fig. 4), and performing calculations between consecutive profiles (e.g., dt in Eq. 3 is the float profiling interval) or as seasonally integrated

270 quantities (e.g., Baetge et al., 2020). The following equation describes the calculations performed at each timestep and in each depth layer

$$NCP(t,z) = (h_{i+1} - h_i)\frac{[T(t_1,z)] - [T(t_0,z)]}{t_1 - t_0} - \Sigma F(t,z) \,. \tag{7.1}$$

275 $NCP(t,z)$ (typically mol T m^{-2} d^{-1}) represents NCP integrated over the depth range $h_{i+1} - h_i$ (m). $[T(t,z)]$ is the average tracer concentration between h_i and h_{i+1}, and $\frac{[T(t_1,z)] - [T(t_0,z)]}{t_1 - t_0}$ is the observed change in the tracer's concentration between time intervals (both mol T m^{-3} d^{-1}). Lastly, ΣF is the sum of the estimated physical fluxes and non-NCP biological terms (mol T m^{-2} d^{-1}). Integrating the resulting NCP values over one year provides an estimate of annual net community production (ANCP; mol T m^{-2} yr^{-1}), which is equivalent to carbon export when integrated to the depth of the maximum annual mixed layer (Yang

280 et al., 2017). However, the depth to which NCP and ANCP estimates are integrated impacts the interpretation and magnitude of the resulting NCP values and metabolic state of the system. Haskell et al. (2020), for example, reported ~10-20% variability in climatological ANCP and monthly NCP estimates calculated down to the seasonal mixed layer depth (MLD), euphotic zone, 100 m, and annual maximum MLD. Pelland et al. (2018) noted ~50% variation in ANCP values when integrating to the seasonal MLD versus 120 m. Ship-based work has also demonstrated the sensitivity of export estimates to the depth of

285 wintertime ventilation, with regions of deep winter MLDs experiencing greater ventilation, and therefore, reduced export or ANCP calculated to that depth (Palevsky et al., 2016).

The general approach represented by Eq. 7.1 has been applied using float-based O$_2$, NO$_3^-$, DIC, TA, and POC observations, although there is significant variability in how and which physical fluxes are included when calculating ΣF, and in how the box model is discretized in time and space (Table 1). Air-sea gas exchange (gases only), vertical and lateral exchange or

290 transport and evaporation/precipitation (excluding O$_2$) are important processes that modify tracer concentrations over daily to monthly timescales (Bushinsky and Emerson, 2015; Emerson and Stump, 2010; Huang et al., 2022; Pelland et al., 2018). Accordingly, ΣF is estimated by calculating some or all of the terms in the following equation,

$$\Sigma F(t,z) = F_{AS}(t,z) + F_{EP}(t,z) + F_{vmix}(t,z) + F_{vadv}(t,z) + F_{ent}(t,z) + F_{horiz}(t,z) + F_{bio}(t,z) \tag{7.2}$$

295

F_{AS} represents gas exchange via bubbles (F_{bub}) and diffusion (F_{diff}) at the air-sea interface, F_{EP} is the evaporation/precipitation flux at the surface, $F_{vmix} + F_{vadv} + F_{ent}$ are vertical transport via diapycnal mixing, advection, and entrainment, respectively, and F_{horiz} is horizontal transport. F_{bio} represents biological processes, not including NCP, such as particulate inorganic C production/consumption, DOC production, or POC sinking, which are reflected in the DIC, TA, and POC budgets (Huang et al., 2022). The general equations for the physical terms in Eq. 7.2 are as follows

$$F_{diff}(t,z=0)=k(t)\left([T(t,0)]-[T(t,0)]_{eq}\right) \tag{7.3}$$

$$F_{bub}(t,z=0)=\beta(F_C(t) + F_p(t)) \tag{7.4}$$

$$F_{EP}(t,z=0)=T{:}S\left(\frac{d[S(t,0)]}{dt}-\frac{d[S(t,0)]}{dt_{phys}}\right) \tag{7.5}$$

$$F_{vmix}(t,z)= \kappa_Z(t,z)\frac{d[T(t,z)]}{dZ} \tag{7.6}$$

$$F_{vadv}(t,z)= w(t,z)\,\Delta[T]_z(t,z) \tag{7.7}$$

$$F_{ent}(t,z)=\begin{cases} \Delta[T]_z\dfrac{dh}{dt}; & \dfrac{dh}{dt} > 0 \\ 0; & \dfrac{dh}{dt} \leq 0 \end{cases} \tag{7.8}$$

$$F_{horiz}(t,z)= u(t,z)\,\Delta[T]_x(t,z) + v(t,z)\Delta[T]_y(t,z) \tag{7.9}$$

where k is the wind speed-dependent diffusive gas transfer coefficient (m d^{-1}), $[T]_{eq}$ is the temperature- and salinity-dependent equilibrium concentration at ambient sea level pressure (mol T m^{-3}), and $F_C + F_p$ represent bubble-mediated gas transfer via small and large bubbles, respectively. The β term is a bubble-flux tuning coefficient between 0 and 1. T:S is the ratio of tracer T to salinity, $\frac{d[S(t,z)]}{dt}$ is the observed change in salinity over time, and $\frac{d[S(t,z)]}{dt_{phys}}$ is the change due to physical processes. F_{diff}, F_{bub}, and F_{EP} are zero below the surface box. The transport terms κ_Z (m^2 d^{-1}), w, dh/dt, u and v (all m d^{-1}) represent the diapycnal eddy diffusivity coefficient, vertical advection velocity, the rate of change of a given depth layer, and the lateral advection velocities, respectively. d[T]/dZ (mol m^{-4}) is the vertical gradient between consecutive depth bins, while $\Delta[T]_z$, $\Delta[T]_x$, and $\Delta[T]_y$ (all mol m^{-3}) represent concentration differences in vertical and horizontal directions.

As summarized in Table 1 and Table A3, different studies have represented the terms in Eqs. 7.3-7.9 in different ways. Parameterizations of air-sea exchange (Eqs. 7.3-7.4) and diapycnal mixing (Eq. 7.6) vary most widely across studies, and those

fluxes typically contribute the largest source of uncertainty in budget-based NCP and ANCP calculations, up to ~40% and 20%, respectively (Bushinsky and Emerson, 2015; Yang et al., 2017; Huang et al., 2022). Different $F_{diff} + F_{bub}$ parameterizations, for example, have been employed, and efforts have been made to tune those terms for local conditions using a scaling coefficient (β). Yang et al. (2017) and Emerson et al. (2019) tuned $F_C + F_P$ for OSP by minimizing differences

330   between observed mixed layer N_2 concentrations and values predicted by the same mass balance used for their O_2-based ANCP calculations. Plant et al. (2016) tuned F_{bub} by scaling the magnitude of that flux to minimize differences between O_2- and NO_3^- -based ANCP estimates. Most recently, Yang et al. (2022) introduced a correction for air-sea flux estimates that relies on reanalysis data products to account for small temperature differences in the ocean skin (the ~500 µm thick layer over which gas exchange occurs) and mixed layer which impact the magnitude of diffusive and bubble-mediated gas exchange. Only that

335   paper and a subsequent one by Emerson and Yang (2022) have applied the correction, but its influence on ANCP estimates may be as large as ~40%. Approaches to estimating the diapycnal mixing flux also differ widely across studies. Most invoke values from the literature, either selecting constant or time-varying climatological κ_Z values for the study region. Bushinsky and Emerson (2015) and Huang et al. (2022) used an average OSP κ_Z time-series from Cronin et al. (2015) for the base of the mixed layer, and scaled values vertically to a background of 10^{-5} m^2 s^{-1} below the thermocline, following Sun et al. (2013).

340   Haskell et al. (2020) scaled the Cronin et al. (2015) κ_Z climatology for their NCP model by minimizing differences between NO_3^-- and DIC-based ANCP estimates. These approaches, however, are somewhat problematic as they likely neglect significant spatial and temporal variability in upper ocean mixing rates. Pelland et al. (2018) derived independent estimates of all the transport terms (κ_Z, w, u, v) by using their glider observations to close heat and salt budgets for OSP, while Plant et al. (2016) estimated the physical transport terms by running locally forced simulations of a Price-Weller-Pinkel (PWP) mixed

345   layer model (Price et al., 1986). Other studies have estimated vertical advection velocities (u) by calculating the Ekman pumping velocity from local wind stress data. Most float-based approaches neglect horizontal transport, suggesting its influence on NCP estimates would be small away from boundary currents, eddies, or frontal zones, and over seasonal timescales, or longer (e.g., Yang et al., 2017; Huang et al., 2018). Emerson and Bushinsky (2015) are the only float-based study to have calculated that term, and found it to be small relative to the vertical physical fluxes, contributing <7% to

350   uncertainty in their ANCP estimates. In a glider-based study, however, horizontal advection fluxes were larger than the sum of all vertical fluxes in the upper 120 and 200 m of the water column (e.g., Pelland et al., 2018). Lastly, entrainment terms, which are often estimated from observed changes in the mixed layer depth or other depth horizons between time intervals, tend to be small, except during periods of rapid mixed layer depth changes.

Different approaches to setting up the vertical discretization have been also applied. For example, Bushinsky and Emerson

355   (2015), Plant et al. (2016) and Pelland et al. (2018) divided the upper water column into multiple depth layers with ~1.5-5 m vertical resolution. Other studies have employed coarser one- or two-box model frameworks, partitioning the upper water column into layers defined by the seasonal or winter maximum mixed layer depth (MLD), euphotic depth, or a fixed density or depth horizon (e.g., Yang et al., 2017; Haskell et al., 2020; Huang et al., 2022). In all cases, the vertical transport and mixing flux terms are evaluated by measuring the depth-dependent change in T (dT/dZ or ΔT_Z) across the base of each box (Fig. 4),

360 and air-sea exchange and/or evaporation are quantified at the top of the surface box, only. There is no consensus on the optimal vertical discretization scheme, and no estimates of the (A)NCP sensitivity to the approach have been reported.

By performing simultaneous NCP calculations using multiple tracers, it is possible to partition biological productivity into distinct biogenic pools, and to estimate other non-NCP biological terms (F_{bio} in Eq. 7.2; Haskell et al., 2020; Huang et al., 2022). For example, while calculations based on O_2 and NO_3^- target particulate and dissolved organic C cycling, those based

365 on DIC or TA are also influenced by inorganic C cycling associated with non-NCP production of calcareous shells by some organisms (Fassbender et al., 2016). Calculations from POC represent only the particulate organic fraction, as well as POC sinking. As a result, differences between DIC, TA, POC, and O_2 or NO_3^- based estimates can be used to quantify sinking rates, and the relative importance of particulate organic, dissolved organic and particulate inorganic production within a system (see details in Huang et al., 2022).

370 Finally, while most NCP studies to date have performed the above calculations at the approximate resolution of the profiling instrument, a handful of studies have evaluated NCP by integrating tracer changes over seasonal timescales (Table A1). Johnson et al. (2017), Bif and Hansell (2019), and Baetge et al. (2020) all estimated NCP as the winter-to-summer drawdown of NO_3^- in the upper 100 m, 75m and 200 m, respectively, neglecting any other NO_3^- sources or sinks (i.e., $h_i - h_{i+1}$ = 100 m, $T(t) = \int_0^{100} \Delta NO_3^- \, dz$ and $\Sigma F = 0$ in Eq. 7.1). A reference winter profile is taken from float observations, and NO_3^- drawdown

375 is converted to C- or O_2-equivalents using Redfield stoichiometry.
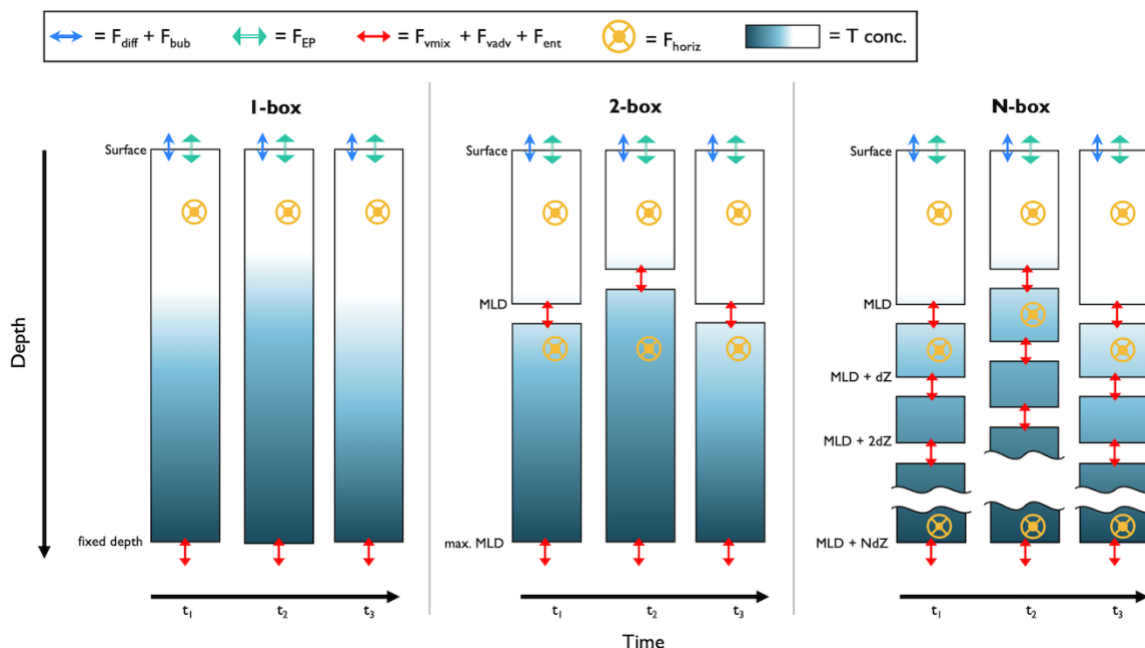
Figure 4 Schematic of box model setups for float-based NCP approaches. The columns represent a profile of tracer observations at discrete time intervals and divided into vertical layers (boxes).

380

Table 1 Variations in budget terms used in float- and glider-based NCP calculations at OSP.

Study	Platform	T	Vertical resolution	$F_{AS} + F_{EP}$ (surface only)	κ_z [m² s⁻¹]	w [m s⁻¹]	dh/dt [m d⁻¹]	u + v [m d⁻¹]
Bushinsky and Emerson, 2015 (BE15)	Float	O_2	N box (0-MLD; MLD-150 m, Δh = 1.5m)	$F_{AS}=k_{O2}$ (O_2-$O_{2,eq}$) + β($F_{bub.}$); β=1, 0.29 (Liang et al., 2013)	Cronin et al. (2015) (surface); Sun et al. (2013) (profile)	Ekman pumping velocity	derived from observations; > 0 only	NCEP/NCAR reanalysis
Plant et al., 2016 (P16)	Float	O_2, NO_3^-	N box (0-180 m, Δh = 2m)	$F_{AS}=k_{O2}$ (O_2-$O_{2,eq}$) + ($F_{bub.}$) (Liang et al., 2013, scaled to NO_3^- ANCP)	1.5x10⁻⁵	PWP	PWP	0
Yang et al., 2017 (Y17)	Float	O_2	2 box (0-MLD; MLD-max. MLD)	$F_{AS}=k_{O2}$ (O_2-$O_{2,eq}$) + β($F_{bub.}$); β = 0.53 (Liang et al., 2013)	1.5x10⁻⁵ (box 2 only)	0	derived from observations; > 0 only	0
Pelland et al., 2018 (P18)	Glider	O_2	86 boxes (0-150 m, Δh = 2m; 150-200 m, Δh = 5m)	$F_{AS}=k_{O2}$ (O_2-$O_{2,eq}$) + β($F_{bub.}$); β = 0.29 (Liang et al., 2013)	T/S budget	T/S budget	0	T/S budget
Haskell et al., 2020 (H20)	Float	NO_3^-	1 box (0- MLD, EuZ, 100 m or max. MLD)	F_{EP}=(dS/dt - dS/dt$_{phys}$) (T:S)	Cronin et al., (2015), scaled to DIC budget	Ekman pumping velocity	derived from observations; > 0 only	0
Huang et al. 2022 (H22)	Float	O_2, NO_3^-, POC, DIC, TA	1 box (0-56 m)	F_{EP} = k_{CO2} (k_H) (ΔpCO_2) + (dS/dt-dS/dt$_{phys}$) (C:S); $F_{AS}=k_{O2}$ (O_2-$O_{2,eq}$) + ($F_{bub.}$) k_{CO2} (Wanninkhof, 2014) $F_{AS,O2}$ (Liang et al., 2013)	Cronin et al. (2015) (surface); Sun et al. (2013) (profile)	Ekman pumping velocity	derived from observations; > 0 and MLD > 56 m, otherwise 0	0

F_{AS} = air-sea gas exchange (mol m⁻² d⁻¹); F_{bub} = air-sea bubble flux (mol m⁻² d⁻¹); F_{EP} = evaporation or precipitation (mol m⁻² d⁻¹); κ_z = eddy diffusivity coefficient [m² d⁻¹]; w = vertical advection velocity [m d⁻¹]; dh/dt = change in layer depth [m d⁻¹]; u + v = horizontal advection velocities [m d⁻¹]; Δh = box vertical displacement ($h_{i+1} - h_i$ in Eq. 7); β = bubble-mediated transfer scaling coefficient [unitless]; PWP = Price-Weller-Pinkel mixed layer model (Price et al., 1986); C:S = observed DIC:salinity ratio [mol C:S].

3 Overview of the current capacity to derive GPP and NCP estimates from BGC-Argo floats

385   Here, we summarize and demonstrate, through examples, the current capacity to determine GPP and NCP using the BGC-Argo array. The main goal of this section is to provide readers with an overview of how the emerging float-based methods are applied. Sections 3.1 and 3.2 demonstrate the methods' applications at local and basin-to-global scales, respectively. In section 4, we discuss the current challenges and opportunity to further broaden the scope of GPP and NCP calculations using floats.

3.1 GPP and NCP calculations at local scales

390

To date, a handful of studies have examined GPP and NCP dynamics at relatively small spatial scales, using data from one or several floats deployed within a single geographic region. Targeted GPP studies employing single BGC-Argo (or BGC-Argo-like) floats have only occurred in the Mediterranean Sea (Barbieux et al., 2022), N Pacific (Henderikx Freitas et al., 2020), and Gulf of Mexico (Gordon et al., 2020). Gordon et al. (2020), however, were unable to reliably determine GOP from their

395   diurnal O_2 curves due to low biological productivity and confounding signals from physical O_2 fluxes. While Barbieux et al. (2022) successfully derived an approximately-four-month euphotic-zone integrated GCP time-series in two locations in the Mediterranean Sea using c_p-POC data, diurnal variations in the b_{bp}-to-POC relationship precluded the same calculations using b_{bp}-POC data.

Float-based NCP studies are somewhat more numerous than GPP studies (Table A2) but are similarly limited in their

400   geographic extent. NCP has been well-studied around Ocean Station Papa (OSP; 50°N, 145°W) in the subarctic NE Pacific (sect. 3.1.1), and only a handful of localized studies have occurred elsewhere, such as in the S. China Sea (Huang et al., 2018) and the NW Atlantic (Alkire et al., 2014; Yang et al., 2021) (Fig. 2c). These studies have spanned from about one year to several, and have employed single floats, or multiple floats clustered within the same region. Plant et al. (2016), for example, used float data from six floats that were deployed independently and consecutively between 2008 and 2013.

405   No single study has examined NCP and GPP dynamics simultaneously, although Alkire et al. (2014, 2012) and Briggs et al. (2018) studied NCP and GPP during the same NW Atlantic spring bloom in their respective papers.

3.1.1 NCP case study at OSP

To demonstrate the current capacity for float-based PP studies at local scales, we performed a case study analysis of float/glider

410   NCP data from OSP. A similar analysis is not presently feasible for GPP, owing to the small number of localized studies using floats and gliders, and the currently insufficient number of profiles available to conduct GPP calculations from composite diurnal cycles.

We compiled all available published float- and glider NCP data collected from OSP between 2008 and 2020. The published data constitute five independent studies, each employing slightly different approaches to quantifying NCP and ANCP (Table

415 1). For comparison with the profiler data, we also compiled independent NCP estimates from ship-board sampling, moorings, and satellites collected over the same timeframe as the float/glider data. We present time-explicit, seasonal average, and annual integrated NCP values integrated to the depth of the annual maximum winter mixed layer (typically ~120 m at OSP), and depth-resolved seasonal average NCP. All values were converted to O_2 equivalents using a PQ of 1.4, and $O_2:NO_3^-$ ratio of 150:-16. Data sources and a detailed description of our data handling are provided in the appendix (Table A1).

420 The compilation of float and glider data from OSP yields a nearly continuous, 12-year time-series of NCP and ANCP estimates, and a shorter, seven-year time-series of depth-resolved estimates (Fig. 5). The temporal resolution of estimates ranges from 10 days (float profiling interval; Plant et al., 2016; Huang et al., 2022) to one month (Pelland et al., 2018). Yang et al. (2017) provided NCP estimates interpolated to one-day resolution, while data provided by Haskell et al. (2020) were averaged over six years. The depth-resolved data from Plant et al. (2016) and Pelland et al. (2018) had vertical resolutions of 2 and 2-5 m,

425 respectively.

There is general consistency in the magnitude (NCP, ANCP) and seasonal patterns (NCP) across the float and glider studies. Most datasets, for example, reveal peak productivity and autotrophy (NCP > 0) between June and August, and minimum values and heterotrophy (NCP < 0) between November and February (Fig. 5a,b). These patterns are also broadly consistent with those of the independent data records. Indeed, the average seasonal float NCP cycle is very similar to the average of ship-based

430 measurements between January and July (compare white and red markers in Fig. 5b), and the seasonality is similar to the average estimates derived from moorings and satellites. Notably, while all float/glider approaches consistently predict periodic net heterotrophic conditions, the satellite-based approaches only ever produce positive NCP estimates, reflecting how those algorithms are trained using only positive PP data (Li and Cassar, 2016; Westberry et al., 2008; Behrenfeld and Falkowski, 1997).

435 The float/glider ANCP estimates are typically within one standard deviation of one another (Fig. 5d). Exceptions to this result are the Huang et al. (2022) O_2-based estimate and the Haskell et al. (2020) NO_3^--based estimate. It is, however, somewhat unsurprising that the Huang et al. estimate exceeds the others because ANCP values from that publication were integrated only to 50 m depth (i.e., calculations integrated to the annual maximum MLD were not available) and may thus exclude subsurface regions of net heterotrophy which occur during the fall and winter (Fig. 5c). For the same reason, it is not surprising that the

440 float- and glider ANCP estimates are typically lower than estimates derived from moorings (Fassbender et al., 2016; Emerson and Stump, 2010), satellites and ships, which only resolve a narrow depth range in the upper ocean.

Despite the general agreement across float- and glider NCP approaches, there are some important differences, which are particularly apparent in the full, time-resolved NCP record (Fig. 5a). For example, NCP estimates made at the same time diverge by up to ~50 mmol O_2 m^{-2} d^{-1}, and in extreme cases, ~100 mmol O_2 m^{-2} d^{-1} across different approaches (Fig. 5a).

445 Likewise, the spread in average seasonal NCP values ~50 O_2 m^{-2} d^{-1} (Fig. 5b). The most notable difference across studies is the anomalous phenology of the Pelland et al. (2018) record, which identifies peak NCP in March, and net heterotrophy in

September and October, only. These differences are also seen in the depth-resolved record from that publication. Interestingly, however, the anomalies in the seasonal record of Pelland et al. (2018) do not correspond with anomalous ANCP.

450   Despite these differences, our analysis demonstrates strong agreement across different float-based NCP studies and illustrates the capacity to derive NCP time-series using consecutive float deployments. In section 4.2, we discuss the factors that contribute to differences in the NCP results presented in Fig. 5.
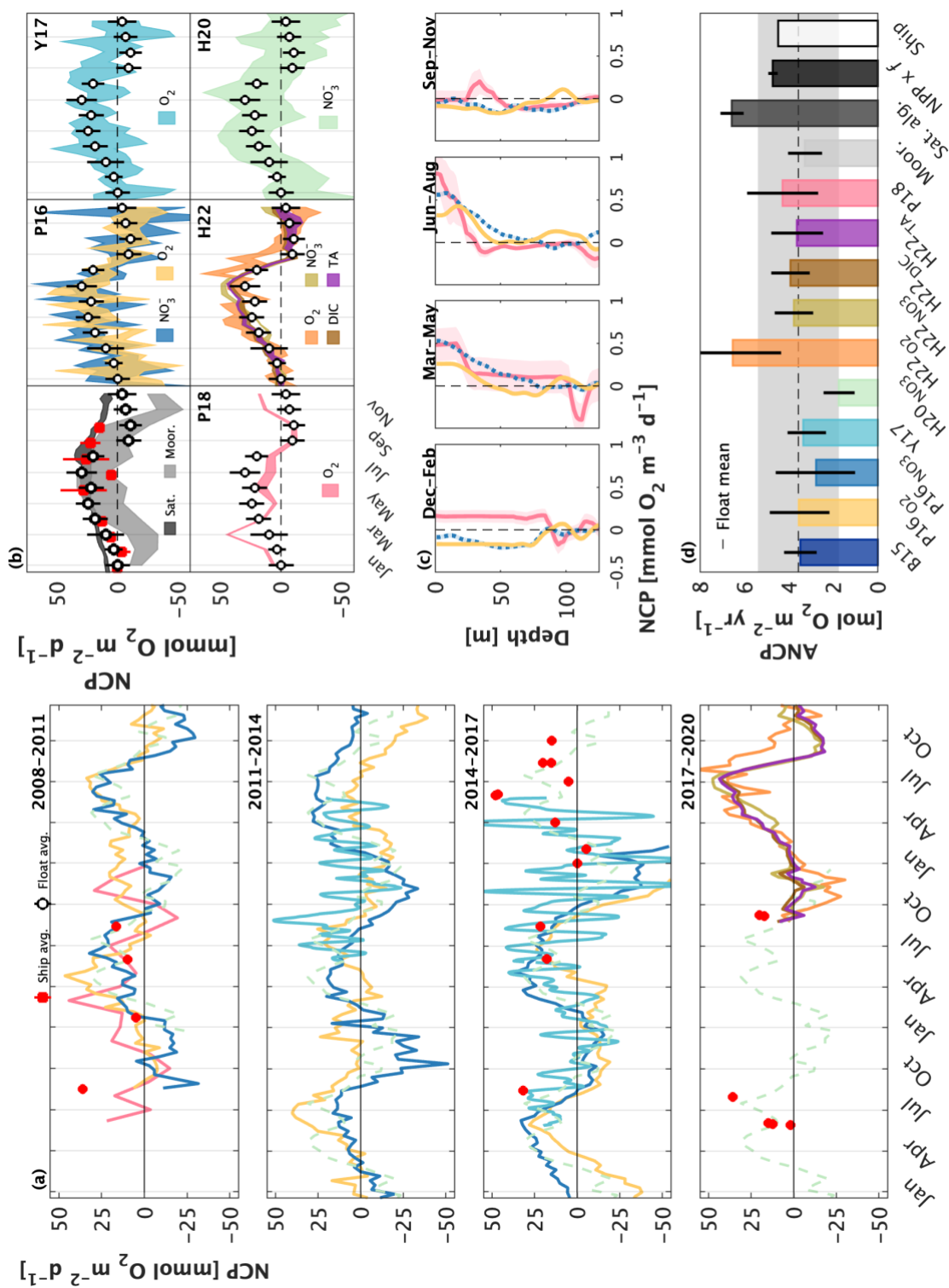
Figure 5 (previous page). Published float- and glider-based NCP estimates from Ocean Station Papa (OSP). (a) Full time-series NCP.
455 **Red markers are ship-based estimates. The H20 record (light green) is dashed because it represents an average annual cycle between 2009 and 2018. (b) Average seasonal cycles, presented at the temporal resolution of each study. Shading around the mean represents the reported approach uncertainty or the standard deviation of estimates derived over multiple years. The black and red markers and error bars represent the average ± one standard deviation annual cycle derived from float and ship sampling, respectively. Depth-resolved NCP estimates in (c) are from Plant et al. (2016; P16) and Pelland et al. (2018; P18). (d) Annual integrated NCP,**
460 **including data from mooring studies (Emerson 2010; 2014; Fassbender et al. 2016; Haskell et al., 2020), a satellite algorithm (Li and Cassar, 2016), a combination of satellite NPP and an empirical estimate of the f-ratio (Westberry et al., 2008; Laws et al., 2011) and ship-based sampling. Colours in (a)-(c) correspond with labels in (b) and (d). Values in (a), (b), and (d) represent quantities integrated to the annual maximum mixed layer depth. The subscripts (e.g., H20$_{NO3}$) denote the tracer used in each study.**

465 ## 3.2 GPP and NCP calculations on basin and global scales

Few studies have examined PP at basin or global scales using float data. Johnson and Bif (2021) provided the first global assessment of decadal GOP and NPP derived from a compilation of float observations, while Stoer and Fennel (2022) presented float-based GPP and NPP estimates of the southern hemisphere ocean. Both studies performed depth-resolved and euphotic zone-integrated calculations by subsetting all available BGC-Argo O_2 and/or b_{bp}-POC data into different geographic regions.
470 Johnson and Bif (2022) performed calculations in 10-degree latitude bands in the Northern and Southern hemispheres, subdividing the data into annual and bi-monthly segments. They also performed calculations at 2-monthly intervals around the Bermuda Atlantic Time-series Station and Hawaii Ocean Time-series sites. Stoer and Fennel (2022), in contrast, performed calculations between 30° and 70°S, only, due to an insufficient number of b_{bp} profiles north of that region at the time.

No studies to date have estimated global NCP from floats. Johnson et al. (2017) (Southern Ocean), Yang et al. (2019), and
475 Emerson and Yang (2022) (both Subtropical Ocean) have, however, provided extensive assessments of (A)NCP from a compilation of multiple floats. Johnson et al. (2017) used BGC-Argo data to characterize ANCP in the Southern Ocean by compiling NO_3^- data from 24 floats deployed between 2009 and 2016. Similarly, Yang et al. (2019) and Emerson et al. (2022) compiled O_2 data from multiple floats to estimate ANCP in the North and South Hemisphere Subtropical Ocean.

No work has simultaneously characterized NCP and GPP at global or regional scales using BGC-Argo data.

480

3.2.1 Global GPP case study

Building on recent work by Johnson and Bif (2021) and Stoer and Fennel (2022), we performed new global GOP and GCP calculations using the available BGC-Argo array. We summarize those calculations here and provide further details in the appendix. Following Stoer and Fennel (2022), we compiled all available high-quality BGC-Argo ΔO_2 and b_{bp}-POC data
485 collected between January 2010 and December 2022. We subset the data into 10 m depth bins, from 0 to 200 m, and different spatial groups, representing 10° latitudinal bands (70°S to 70°N) or Longhurst Biogeographical Provinces (Longhurst, 2006; Flanders Marine Institute, 2009). We constructed composite diurnal curves in each spatial subset by calculating the median ΔO_2 or b_{bp}-POC value at each hour of the day. We subsequently calculated GPP by fitting a sinusoidal function to the resulting

diurnal curves (sect. 2.1). We accounted for DOC production by scaling b_{bp}-GPP estimates by a global mean PER value of
490   33% (Moran et al., 2022), and converted GCP to O_2 equivalents using a photosynthetic quotient of 1.4 (Laws, 1991) (i.e.,
$\frac{b_{bp}\text{-}GCP}{1\text{-}0.33}$ 1.4).

These calculations yield spatially explicit, depth-resolved ΔO_2-GOP and b_{bp}-GCP estimates, representing a median snapshot
from 2010 to 2021. Our calculations, we extend the work of Johnson and Bif (2021) and Stoer and Fennel (2022) by 1)
attempting simultaneous ΔO_2-GOP and b_{bp}-GCP calculations in different biogeochemical provinces and latitude bands of
495   northern and southern hemisphere waters, 2) comparing the float-based data to archived GOP datasets (Table A1), and 3)
assessing the availability of float profiles to perform GPP calculations.

We compiled a total of ~222,300 O_2 and ~103,800 b_{bp} profile observations. After discarding data from floats that did not
profile all hours of the day evenly (i.e., floats that sampled at integer intervals, 5- or 10-day) only ~23% (O_2) and 24% (b_{bp}) of
the original datasets were available for our GPP calculations (compare dashed and solid lines in Fig. 6a). This processing also
500   resulted in significantly more O_2 and b_{bp} profiles in the Southern Ocean, and typically fewer than 1000 b_{bp} profiles in each
latitude band or province in the northern hemisphere.

We were able to derive GOP estimates in 26/32 non-coastal provinces and 12/14 latitude bands, and GCP in 11/32 provinces
and 4/14 latitude bands (Fig. 6b). GCP calculations were not feasible in most northern latitude regions due to an insufficient
number of profiles, based on thresholds estimated in Johnson and Bif (2021) and Stoer and Fennel (2022). Among the regions
505   with sufficient profiles, ~32% and 20% of the dataset had negative or unrealistic O_2- or b_{bp}-GPP values, resulting from poor
detection of a diurnal curve. In waters shallower than 60 m, these values decrease to ~19 and 17%, respectively, owing to the
observation of more pronounced photosynthesis in surface waters.

There is generally good agreement between float O_2- and b_{bp}-based GPP and between the float estimates and independent GOP
estimates derived from bottle sampling (Fig. 6b,c). These results are best seen in surface waters and in vertical profiles of the
510   Southern Ocean. We did directly not compare the vertical profile float-GPP values against independent bottle samples due to
the increasing errors in float GPP with depth. There is also reasonable agreement between our O_2-GOP calculations in surface
waters (<20 m) and those reported in Johnson and Bif (2021) (yellow line in Fig. 6b). The median difference between our
estimates and those of Johnson and Bif (2021) was ~-0.2 mmol O_2 m^{-3} d^{-1}, on average (range -0.7-1.6 mmol O_2 m^{-3} d^{-1}),
excluding latitude bands centred at between 5° and 15°S, where there were too few profiles for Johnson and Bif (2021) to
515   derive estimates. At those latitudes, we were able to derive GOP estimates, but the resulting values have high uncertainty
(shading in Fig. 6b), owing to the small number of profiles (~600 at both latitude bands) in that region. The low number of
profiles and high uncertainty in the low-latitude regions likely also explain the offset between our float-based GOP, and the
archived data in that region. We suspect that once more profiles are collected, we will see stronger agreement between the
float- and ship-based estimates.

520   It is also noteworthy that depth-resolved GPP values derived using the sinusoidal, linear, and P-vs-E algorithms agree within
one standard error of the approach for both O_2 and b_{bp}-based estimates (Fig. 6c). In the upper 100m for the region of 30-70°S,

the average range of GPP values derived using the three algorithms was only 0.4 and 0.1 mmol O_2 m^{-3} d^{-1} for O_2- and b_{bp}-based estimates, respectively.

Overall, the histogram distributions of the float-based GPP estimates demonstrate broad agreement between float and bottle-525   sample GPP estimates, at all depths shallower than 100m (Fig. 6d). The distributions suggest that float-based, decadal estimates are within the range of expected values derived from bottle sampling, albeit with a slight tendency for lower estimates in the float dataset (median float-based O_2- b_{bp}- and archived-GPP values of 0.7, 0.5, 1.3 mmol O_2 m^{-3} d^{-1}, respectively). This result, however, is unsurprising as diurnal cycles derived from a composite of observations obtained over multiple years will also have dampened amplitude relative to daily cycles observed over a single day or composited over a single season. This result
530   may also reflect a high proportion of negative or undetectable GPP values in the float dataset, and a summertime (i.e., high-GPP) sampling bias in the bottle sample record (~65% of the dataset).

In summary, of GPP case study results demonstrate 1) the general insensitivity of calculated GPP values to how the diurnal cycle is constructed (i.e., median binned, as in Stoer and Fennel, 2022, or unbinned as in Johnson and Bif, 2021); 2) that different GPP algorithms give similar results, although the sinusoidal fit tends to have the smallest error; 3) the robustness of
535   the decadal GPP estimates to the addition of new profiles since calculations were performed by Johnson and Bif (2021) using data available up to 2021; and 4) that float-based GPP estimates are within the range of expected values.
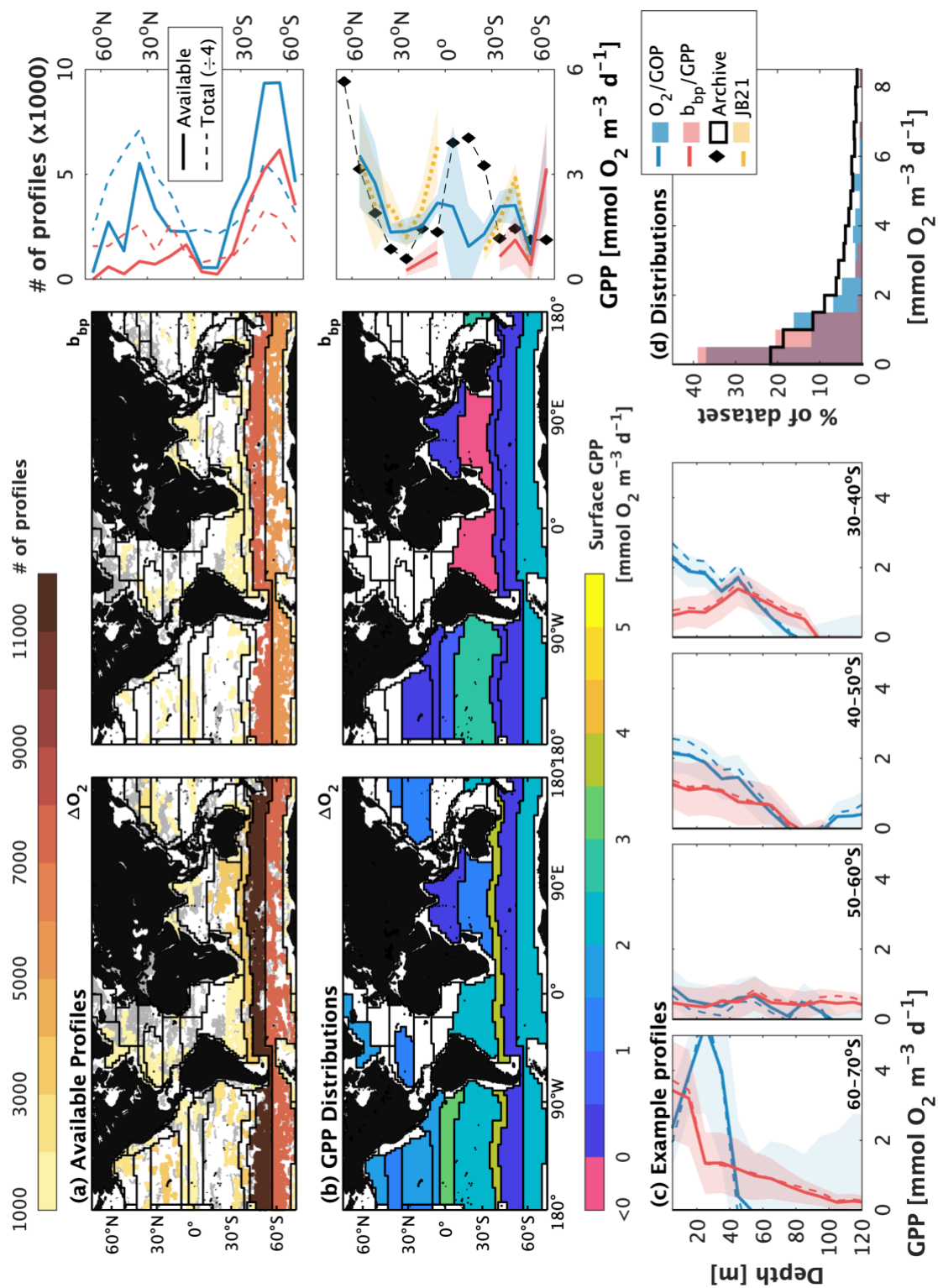
540 **Figure 6 (previous page). Demonstration of global-scale float-based GOP and GCP estimates. (a) shows the distribution of BGC-Argo profiles, collected between January 2010 to December 2022 that are available for GOP or GCP calculations in Longhurst Biogeographical Provinces or by latitude. The coloured markers in the maps represent the profile locations of floats that sample all hours of the day evenly, while the grey markers represent profiles obtained from floats that do not. The colour identifies the total number of profiles in each province, whose boundaries are identified by the black lines. In the latitudinal distribution, the solid line**
545 **represents the number of profiles available for GPP calculations, and the dashed lines represent the total number of profiles collected (divided by four, for comparison), including those from floats that did not sample all hours evenly. Panel (b) shows the distribution of surface (0-20 m average) GPP estimates by province or latitude band. Regions without data reflect an insufficient number of profiles available for calculations. Panel (c) shows an example of vertical GPP profiles in the southern hemisphere, and (d) shows the histogram distribution of float-based, and archived GOP data, derived from ship bottle sampling at all latitudes in waters**
550 **shallower than 100 m. In panels (b) and (d), the black markers/lines represent archived bottle-sample GOP data, median-binned by latitude band, and the yellow line represents ΔO_2-GOP estimates from Johnson and Bif (2021; JB21). The thin dashed lines in (c) are GOP estimates derived using the linear and P-vs-E algorithms; the solid lines are from the sinusoidal algorithm. Throughout, POC-based GCP estimates were converted to O_2 equivalents using a PQ of 1.4 and DOC production of 33%.**

4 Discussion

555 ### 4.1 Constraints on GPP accuracy and coverage

Float-based GPP estimates have been shown to compare well with independent data, and well between O_2- and POC-based estimates (see our global GPP case study, sect. 3.2, also Johnson and Bif, 2021; Stoer and Fennel, 2022). However, we do not observe an expected ratio between ΔO_2-GOP and POC-GCP values when compared directly for co-located profile observations (Fig. 7). Given an estimated range of ~18-47% DOC production during photosynthesis (median PER value of 32.5% ± 14.4%

560 standard deviation calculated from Moran et al., 2022), and a PQ range of 1-1.45 (Laws, 1991), the ratio between ΔO_2-GOP and POC-GCP uncorrected for PER should be between ~1.2 and 2.6 (shaded region in Fig. 7). Considering an even broader PER range of ~2-50% (global confidence interval from Baines and Pace, 1991) results in an expected GOP:GCP ratio of ~1-2.9. In our depth-resolved, global GPP dataset, we derived a median ratio of ~3.1 ± 0.2 (median ± confidence interval) for estimates derived in the upper 60 m. When considering all depths (up to 200 m), the median ratio is ~4.1 ± 0.6, reflecting the

565 lower signal-to-noise ratio of diurnal O_2 or b_{bp} variability at depth. For comparison, Briggs et al. (2018) calculated a ratio of ~2.6 between mixed layer O_2-GOP and c_p-GCP during a NW Atlantic spring bloom. These results imply higher PQ values and/or DOC production rates and may indicate that these terms are non-uniform across the global ocean. Using static PQ or PER values in GPP calculations (as in Stoer and Fennel, 2022 and in our global GPP case study) likely contributes to the uncertainty in the resulting GPP datasets, and partially explains the offsets we observed O_2- and POC-based GPP estimates,

570 and differences between the float- and bottle sample GPP values. Other sources of uncertainty are discussed in the following paragraphs.

Diurnal cycle GPP methods are based on the presumption that day-night variations in photosynthesis are the primary driver of diurnal variations in upper ocean O_2 or POC concentrations. Other than accounting for potential diurnal solubility impacts on O_2 (through expressing O_2 as its concentration anomaly, ΔO_2) no attempts have been made to reconcile for additional diurnal

575 variations in float O_2 or POC observations that are not caused by photosynthesis. For O_2, these include potential impacts due to air-sea exchange or vertical mixing, and for POC, sinking, grazing, or PER. Yet, these processes vary throughout the day,

and the extent to which they do changes seasonally and geographically. Diurnal variability in solar heating and wind forcing influence mixed layer dynamics on hourly, or longer, timescales, with impacts on air-sea gas exchange (Briggs et al., 2018) and near-surface vertical mixing (Price et al., 1986). Moreover, particle sinking, grazing, or DOC production, have been

580 implicated as a mechanism for decoupling O_2- and POC-based PP estimates, particularly in high-productivity (e.g., diatom-dominated) regions (e.g., Rosengard et al., 2020). For example, regions of high POC sinking rates, grazing or PER will decouple O_2 and POC concentrations, leading to observations of high-O_2 and low-POC in upper ocean waters, with implications for resulting GPP and CR estimates (White et al., 2017; Rosengard et al., 2020; Briggs et al., 2018). Independently or in combination, these processes likely imprint on the daily signals detected by BGC-Argo floats, whether by single assets

585 or the composite of the array, and therefore constitute a source of uncertainty to the resulting GPP estimates.

The use of POC to estimate GPP also requires the assumption that gross community production is equal to autotrophic gross carbon production (White et al. 2017; Henderikx Freitas et al., 2022; Stoer and Fennel, 2022), and that daily cycles of non-algal particles are negligible. Often, however, this may not be the case. Moran et al (2022) suggested that bacterial carbon production contributes a small, but highly variable, fraction to particulate PP, equal to ~13±19% (mean ± one standard

590 deviation), or <10% of total PP if PER is ~30%. For the size range relevant to b_{bp}, Martinez-Vincente et al. (2012) further suggested that the variability in b_{bp} largely results from variability in phytoplankton between 2 and 20 μm in diameter, despite the majority of the b_{bp} signal coming from highly abundant bacteria. Thus, if diurnal variability in b_{bp} is mainly attributed to phytoplankton, then the b_{bp} daily signal may still be a close proxy of GPP. Nonetheless, it is important to consider other potential sources of variability in b_{bp} attributed to non-algal particles.

595 Variations in the b_{bp}-to-POC relationship, both in space and in time, also contribute a key source of uncertainty in the POC-based GPP estimates. Several algorithms between b_{bp} and POC exist, including the global algorithm of Graff et al. (2015) and several regional ones (e.g., Loisel et al., 2011; Cetinić et al., 2012). We, and Stoer and Fennel (2022) used a b_{bp}-to-POC relationship based on a globally distributed dataset, which may not be appropriate for all ocean regions or depths (Bol et al., 2018). Moreover, diurnal variations in the b_{bp}-to-POC relationship have been implicated in the uncertainties in b_{bp}-POC-based

600 GPP estimates in the Mediterranean and NW Atlantic (Briggs et al., 2018; Barbieux et al., 2022). Such variations may be attributed to changes in the phytoplankton carbon-to-b_{bp} ratio (Poulin et al., 2018) or refractive index (Henderikx-Freitas et al., 2022), which will confound interpretations of particulate productivity. Beam attenuation-based GCP estimates (c_p-GCP), however, appear to be more reliable than those derived from b_{bp} due to the dampened diurnal variability in the c_p-to-POC relationship (Briggs et al., 2018; Barbieux et al., 2022). At this time, though, c_p is not widely measured on BGC-Argo floats,

605 and a far greater proportion of BGC-Argo floats already measure b_{bp}.

Differences in sampling time and location, including offsets in the number and locations of O_2 versus b_{bp} profiles, will also contribute to uncertainty in GPP comparisons. This includes differences between the timing and locations of independent bottle samples (see markers in Fig. 1) and float profiles, as well as differences in the timing and location of float O_2 and b_{bp} profiles. For these reasons, it is not surprising that the relationship between ΔO_2-GOP and b_{bp}-GCP is less robust when considering the

610 non-co-located float profiles (data not shown).

Finally, a critical number of profiles are needed to accurately estimate GPP from daily cycles of composite float profiles. As mentioned here and in previous studies (Johnson and Bif, 2021; Stoer and Fennel, 2022), a large number of floats are discarded from calculations because they do not sample all hours of the day evenly, presently reducing the number of profiles available for GPP calculations by ~75%. As a result, calculations are precluded in many regions or latitude bands, particularly those

615   based on b_{bp}, and the resulting values are likely less robust. In the N Atlantic Ocean, for example, many floats currently do not sample all hours of the day evenly (compare grey and coloured markers in Fig. 6a), preventing GPP calculations in a number of provinces in that region. For this method to be applied more broadly, floats need to cycle at all hours of the day. To achieve this, float manufacturers should ensure that the sampling protocols can be readily adjusted to the recommended profiling interval of 5.2 or 10.2 days by users via the float firmware. We discuss, in more detail, the minimum number of floats required

620   for robust GPP calculations in the following section.
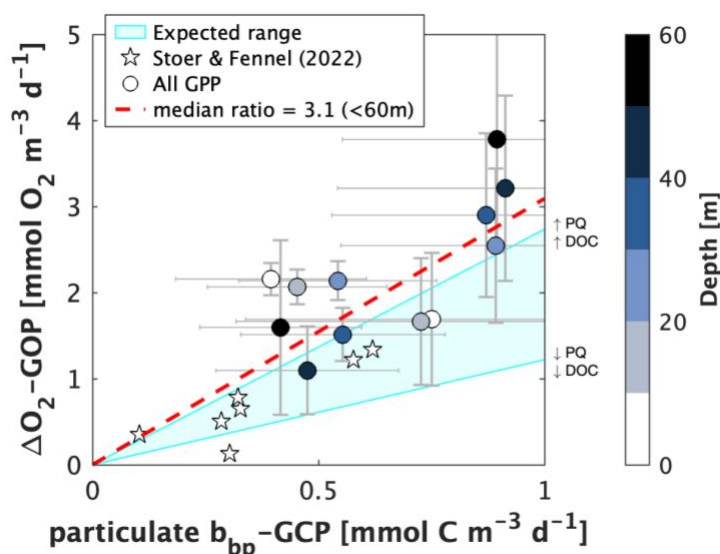
Figure 7. A comparison of depth-resolved ΔO_2-GOP and bbp-GCP estimates in waters shallower than 60 m. Data points represent values derived from co-located profiles in latitude bands or Longhurst Provinces with enough profile measurements to obtain
625   **statistically consistent GPP estimates (sect. 4.1.1). Error bars represent one standard error. Star markers represent GPP estimates from Stoer and Fennel (2022) which were obtained from co-located O_2 and b_{bp} profile measurements below the euphotic depth in the latitude range 30-60 °S. GCP estimates were not converted to O_2 equivalents, nor were they adjusted for potential PER. The light blue shading represents the expected range for the relationship between GOP and GCP, given a PER range of 18-47% (Moran et al., 2022) and PQ range of 1-1.45 (Laws, 1991). The dashed line shows the median GOP:GCP ratio below 60 m.**

630

4.1.1 How many floats are required for consistent, annual GPP estimates?

Following Stoer and Fennel (2022), we performed a bootstrapping analysis to determine the number of O_2 and b_{bp} profiles required to obtain stable GOP or GCP estimates in different latitude bands. We performed the analysis in the 0-30° and 30-

60ºN/S latitude bands for O_2-GOP and in the 0-30ºN and 30-60ºS regions for b_{bp}-GCP. There are not enough b_{bp} profiles currently available to perform the calculations outside of those regions. In each band, we calculated GPP from diurnal cycles constructed from a random subset of data, repeating calculations 1000 times for subset sizes between 500 and 12,000 profiles. As above, we did not sub-sample the profiles in time, such that our GPP estimates reflect an ensembled median value over the period of 2010-2022. From the resulting GPP estimates, we calculated the 0-100 m integrated quantities, and we derived a signal-to-noise ratio by dividing the standard deviation by the mean value. Unlike Stoer and Fennel (2022), who used a threshold ratio of one, we determined the minimum number of profiles required as the first subset size with a ratio less than 0.5.

Our calculations suggest that between 500 (0-30ºN) and 6500 (30-60ºS) O_2 profiles, and between 1100 (0-30ºN) and 4500 (30-60ºS) b_{bp} profiles are required to obtain robust annual GPP estimates from composite diurnal cycles (Fig. 8a,b). Previous estimates are somewhat lower: 20 or 50 O_2 profiles per hour (480 or 1200 per day composite day) in tropical and high-latitude waters, respectively (Johnson and Bif, 2021), or 5000 O_2 and 2000 b_{bp} profiles south of 30ºS (Stoer and Fennel, 2022). Regardless, these results imply that the horizontal and/or temporal resolution of GPP estimates derived from composite sampling is presently constrained by the number of floats available to attain the requisite number of profiles. While the total number of profiles collected by the BGC-Argo array since 2010 is sufficient to derive decadal O_2-GOP, but not b_{bp}-GCP, from composite daily cycles in most 10º latitude bands (compare solid lines and shaded region in Fig. 8a,b), more floats will be required to perform similar calculations in narrower latitude bands, or biogeographic provinces. More floats are also necessary to yield GPP estimates with better-than ~10-year temporal resolution.

Notably, our results indicate that the projected array of 1000 BGC-Argo floats (Roemmich et al., 2021; Biogeochemical-Argo Planning Group., 2016) should be sufficient to obtain annual, or better, GPP snapshots at most latitude bands. Assuming, for example, that the projected 1000-float array is deployed evenly in proportion to ocean surface area in each latitude band, and that floats profile every 10.2 days, then the number of profiles obtained per year (dashed black lines in Fig. 8a,b) will be greater than the minimum threshold that we calculated in our bootstrapping analysis at many latitudes. Given these assumptions, there would be enough profiles to obtain sub-annual GPP estimates in regions equatorward of ~30ºN/S (dashed lines in Fig. 8c). More floats will be required towards the poles, although the achievable temporal resolution may still be less than two years in high-latitude Southern Ocean waters. This resolution cannot be achieved if floats are set to cycle at integer intervals (sect. 3.2.1), but, in theory, if all floats are set to profile every 5.2 days (rather than 10.2 days), the duration to achieve the minimum profile threshold should be halved. Given the current BGC-Argo array, on the other hand, the best-available temporal resolution is typically greater than one year at all temperate or sub-polar latitude bands, but may be less than one year in the tropics and sub-tropics (solid lines in Fig. 8c).

It is also noteworthy that our estimates of the minimum number of profiles required for consistent GPP estimates are based on the compilation of ΔO_2 or b_{bp} data obtained during all months of the year. Towards the poles, the amplitude and phase of diurnal productivity or biomass cycles differ between seasons, due, in part, to light constraints on productivity. The diurnal cycles constructed from a composite of measurements obtained throughout the year reflect somewhat conflicting signals from

sampling at different times of year, making it more difficult to resolve a clear diurnal signal. As a result, it is likely that our threshold estimates represent an overestimate of the number of profiles required to obtain consistent seasonal GPP values in

670 some regions. Unfortunately, however, there are an insufficient number of profiles presently available in a given season to repeat the analysis at higher temporal resolution.
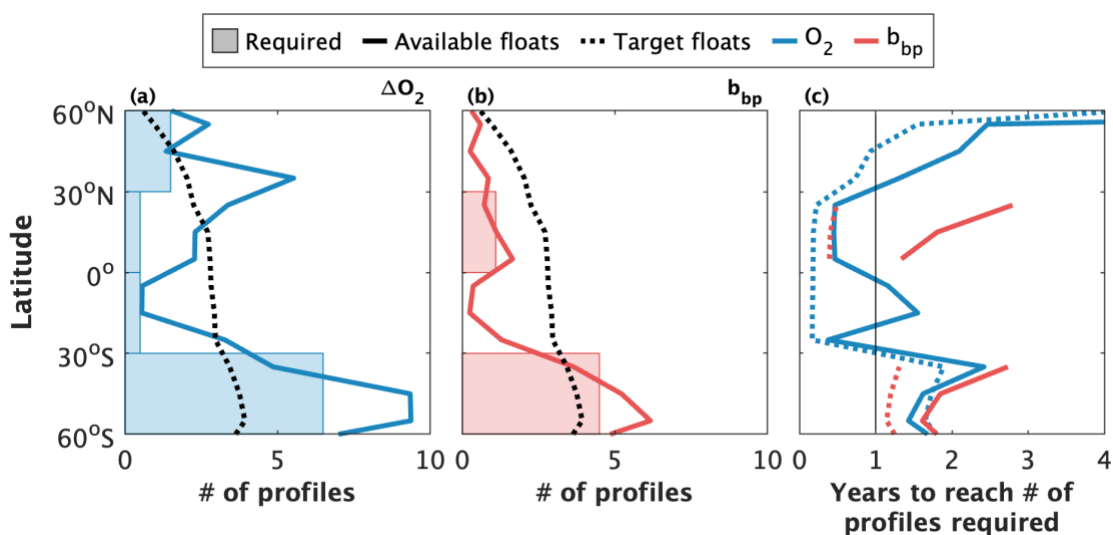
Figure 8. Estimates of the number of profiles and time required to derive statistically consistent GOP and GCP estimates at different
675 **latitude bands. The shaded regions in (a) and (b) represent the estimated number of profiles required for O_2 and b_{bp}, respectively. The minimum number of profiles required was calculated from a bootstrap analysis with a signal-to-noise threshold of 0.5. The solid lines represent the current number of profiles available for GPP calculations since 2010. The dashed lines represent estimates of the number of profiles obtained, per year, by a target BGC-Argo array of 1000 floats deployed ocean-wide proportionally with ocean surface area, and profiling at 10.2-day intervals. Panel (c) shows an estimate of the time required to attain the minimum number of**
680 **required profiles if the current active (Jan. 2023; solid lines) and target (dashed lines) BGC-Argo arrays profile at 10.2-day intervals. The time required was calculated as $\frac{(\text{profiles required}) \times (10.2 \text{ days per profile})}{(\text{current or target \# of floats in region}) \times (365 \text{ days per year})}$.**

4.2 Constraints on NCP accuracy and coverage

The compiled OSP NCP time-series (Fig. 5, sect. 3.1) identified important differences between float-based NCP studies. Those
685 differences can be attributed to one of the following: 1) real, interannual NCP variability, 2) the tracer used to evaluate the NCP budget, or 3) the budget setup and parameterizations. We used the compiled OSP results to assess the potential role of each of those factors on time-resolved and annual-integrated NCP (Fig. 9a). To assess the natural interannual variability, we calculated the mean range of monthly NCP or annual ANCP across studies spanning multiple years (Plant et al., 2016; Yang et al., 2017). To determine the impact of tracer selection, we calculated the mean monthly range of values across studies that
690 performed calculations using more than one tracer (Plant et al., 2016; Huang et al., 2022). And to determine the role of the

parameterization approach, we calculated the mean monthly range of values across all O_2-based studies (Plant et al., 2016; Yang et al., 2017; Pelland et al., 2018) occurring within the same year.

Our analysis suggests that interannual NCP or ANCP variability is the largest contributor to differences between the float-based OSP NCP studies (Fig. 8a,b). Between-tracer and between-approach differences are similar in magnitude for time-695   resolved NCP estimates, but between-approach differences are smallest across ANCP estimates. Interannual differences are largest in the early spring, which may reflect year-to-year differences in the onset of the spring bloom, or the end of wintertime heterotrophy. There are no apparent seasonal patterns in the between-tracer or between-approach differences, although between-tracer differences are somewhat smaller during the summer.

As described in section 2.1, between-tracer differences reflect how the tracers target different components of the carbon pool 700   and system (Huang et al., 2022). Calculations based on O_2 and NO_3^- reflect particulate and dissolved organic C cycling, while POC-based calculations only reflect the particulate organic fraction. DIC or TA budgets, meanwhile, are influenced by organic and inorganic C cycling. Differences between O_2 and NO_3^--based estimates, moreover, are sensitive to the relative importance of new production (based on NO_3^-) versus recycled production (based on NH_4^+), and, to a lesser degree, N_2-fixation. It is possible to partition some of the processes and carbon pools by performing simultaneous NCP calculations using multiple 705   tracers (Huang et al. 2022), but in the absence of such calculations, it is important to consider how the tracer selection influences the interpretation of NCP results. In addition, the between-tracer differences also somewhat reflect the importance of different flux parameterizations used in the budget calculations. For example, calculations based on O_2 require estimates of the air-sea flux term, while those based on NO_3^- do not. As a result, those estimates based on NO_3^- may be perceived to be somewhat more accurate, due to the large air-sea flux uncertainties (e.g., Bender et al., 2011; Emerson and Bushinsky, 2016).

710   The between-method differences reflect differences in the flux parameterizations and NCP budget setup between studies, which are summarized in section 2.2 and Table 1. We examined the contributions of different fluxes to the overall differences between approaches by calculating the range of physical fluxes (air-sea, vertical mixing, entrainment, and vertical advection) applied in the different studies at OSP (Fig. 9c,d). To estimate the range of air-sea fluxes represented in the OSP studies, we calculated monthly average surface water O_2 and $O_{2,eq}$ using BGC-Argo observations collected from OSP between 2008 and 715   2020. We then applied the different O_2 air-sea flux parameterization schemes (Table 1) and calculated the resulting range of values. Similarly, we used BGC-Argo observations to the range of vertical fluxes by determining the average monthly subsurface vertical O_2 gradient (d[T]/dZ in Eq. 7.6) and concentration difference ($\Delta[T]_Z$ in Eqs. 7.7, 7.8), and multiplied those values by the different eddy diffusivity (κ_Z), vertical advection (u) and entrainment (dh/dt) values applied in the OSP studies. Our analyses indicate that the air-sea flux and vertical mixing fluxes are the most variable across studies, contributing large 720   uncertainty in time-resolved and annual integrated NCP (Fig. 9c,d). Previous work has similarly identified air-sea flux and eddy diffusive mixing as two of the most important sources of uncertainty in their ANCP calculations, up to ~0.7 and 0.3 mol $O_2 \, m^{-2} \, yr^{-1}$, respectively (Bushinsky and Emerson, 2015; Plant et al., 2016; Yang et al., 2017). Moreover, Plant et al. (2016) estimated an ANCP range of nearly 2 mol $O_2 \, m^{-2} \, yr^{-1}$ when applying different air-sea flux parametrizations to their calculations,

and a range of ~1 mol O_2 m^{-2} yr^{-1} was calculated between ANCP estimates derived using regionally tuned versions of the Liang
725   et al. (2013) air-sea flux model, and an un-tuned version (Plant et al., 2016; Yang et al., 2017).

Another important constraint on the accuracy of float-based NCP estimates is the measurement accuracy of the BGC variable. A ±1% error in O_2, for example, can contribute between 0.3 and 2 mol O_2 m^{-2} yr^{-1} uncertainty to ANCP estimates (Bushinsky and Emerson, 2015; Yang et al., 2017; Huang et al., 2018), comparable in magnitude to uncertainties resulting from air-sea flux and diffusive mixing. Plant et al. (2016) also found that a ±1% O_2 error results in ~±10 mmol O_2 m^{-2} d^{-1} error in time-
730   resolved NCP, and, in some cases, causes a shift in the apparent upper ocean metabolic state (i.e., a shift between net heterotrophy and net autotrophy), particularly during the transition seasons. In some cases, erroneous float data should preclude NCP calculations altogether (Plant et al., 2016), and, in general, NCP calculations cannot be performed reliably on unadjusted BGC-Argo data.

It is noteworthy that our analysis does not reveal which methods are most accurate. Rather, our analyses were intended to
735   identify sources of variability across NCP studies. Moreover, our case study focused exclusively on OSP, which is well studied with respect to upper ocean mixing fluxes (Cronin et al., 2015), air-sea exchange (e.g., Emerson and Bushinsky, 2016; Emerson et al., 2019; Steiner et al., 2007; Vagle et al., 2010) and NCP. That many other ocean regions are not so well characterized may ultimately limit the current capacity to derive accurate float-based NCP estimates. Future work should thus endeavour to better understand the relative importance and magnitude of the physical fluxes in a variety of ocean regions. In doing so, efforts
740   to tune air-sea flux parameterizations for regional conditions (e.g., Plant et al., 2016; Yang et al., 2017; Emerson et al., 2019; Haskell et al., 2020), or to identify the most accurate parametrization in different basins (e.g., Atamanchuk et al., 2020) should be undertaken. Approaches like the one employed by Pelland et al. (2018) to evaluate the physical mixing terms from temperature or salinity budget calculations based on in situ profiler data should also be made alongside corresponding NCP budget calculations.

745
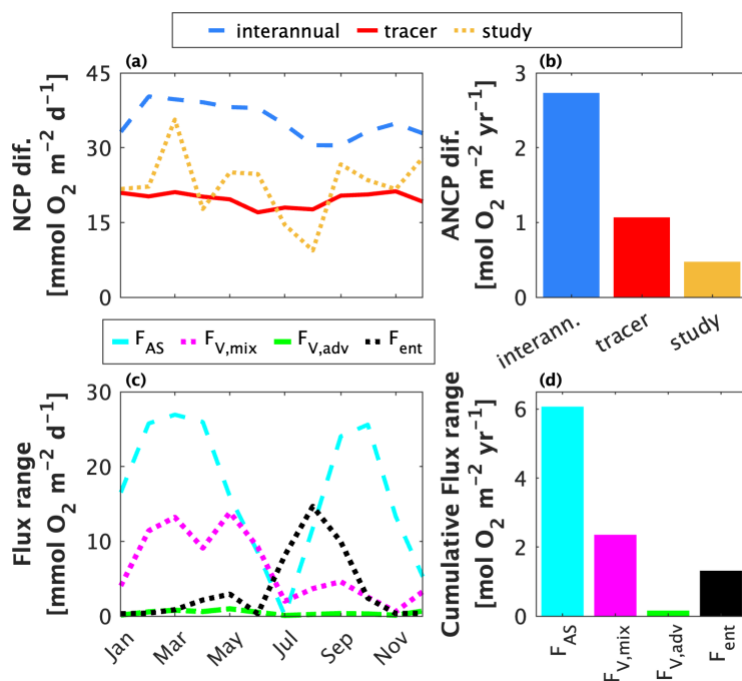
Figure 9. Contributions to differences between float-based NCP and ANCP estimates at OSP. Panels (a) and (b) show estimates of the contributions of different factors to differences in published ML-integrated NCP and ANCP estimates from OSP. The blue line/bar represent differences due to real, interannual NCP and ANCP variability; the red line/bar shows differences resulting from the choice of tracer; and the yellow line/bar represents differences between approach occurring between studies within the same year. Panels (c) and (d) represent estimates of the range of O_2 flux parameterizations across studies (Table 1). For each flux, values were calculated as the absolute range of estimates after applying the different parameterizations for each term (Table 2). Panel (d) shows the cumulative flux range over one year.

5 Conclusion

The BGC-Argo fleet offers global observations of real-time ocean biogeochemistry, enabling widespread PP measurements that are independent of, yet complementary to satellite and ship-based approaches. However, compared with PP methods that rely on traditional sampling infrastructure, float-based methods confer significant advantages to detecting PP. Float-based methods, for example, provide simultaneous horizontal, vertical, and temporal PP coverage, presenting the opportunity to fill key gaps in the existing PP data record (Fig. 1). Moreover, float data and float-based PP methods are publicly available, enabling cost-effective PP calculations that can be independently verified and applied by the entire science community, including those without the resources to perform traditional PP methods. Lastly, float-based methods facilitate enhanced detection the biological response to unpredictable or episodic events like wildfires, volcanic eruptions, or bloom periods, which often cannot be sufficiently characterized using traditional in-situ datasets (Tang et al., 2021).

As float-based techniques mature, the BGC-Argo fleet can be used to extend our current understanding of the marine GPP, NPP, NCP, and C-export, particularly at scales that have so far only been achieved through satellite-based algorithms (e.g.,

Behrenfeld and Falkowski, 1997; Laws et al., 2011). For example, by compiling the data discussed and derived in this paper, we can calculate independent, global estimates of the carbon export ratio (equivalent to ANCP divided by NPP, where NPP is derived from float-GOP; Figure 10). Notwithstanding the regional and temporal biases in current float-based PP estimates,

770 these C-export ratio estimates are consistent with the commonly used satellite models of Laws et al. (2011) and Henson et al. (2012). Moving forward, the extent to which float-based PP calculations can applied will depend, to a large degree, on the availability of float data (sect. 4.1.1), and our capacity to better constrain key sources of uncertainty in biogeochemical budget interpretations (sect. 4.1 and 4.2). Indeed, to increase the availability of float-based PP data, expansion of the Argo fleet should be prioritized, particularly in under-sampled ocean regions. Floats will need to be deployed with sampling intervals set to 5.2

775 or 10.2 days (rather than 5.0 or 10.0 days) to properly detect diurnal variability. Finally, fully exploiting floats for PP measurements will rely on the open availability of PP datasets, including processed data and relevant software.

Ultimately, increasing the availability of in situ PP datasets will convey tangential benefits, like the ability to improve numerical model predictions through data assimilation (e.g., Wang et al., 2020a) and to train satellite PP algorithms, as has been done previously using ship data (e.g., Li and Cassar, 2016; Huang et al., 2021). Doing so will enable unprecedented, in

780 situ classification of the response and variability of marine PP to various environmental perturbations over a range of space and time scales.
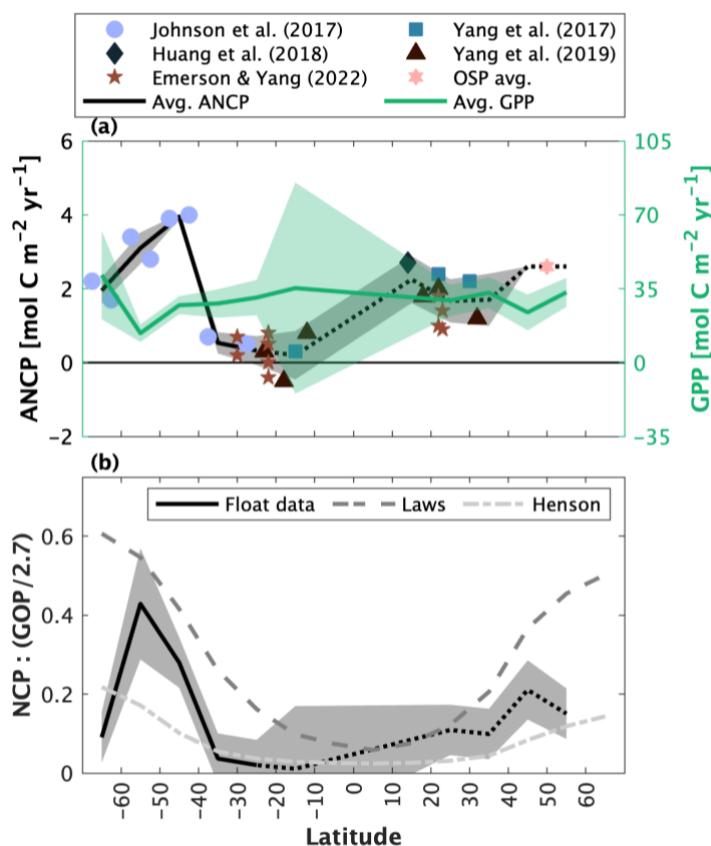
Figure 10. The latitudinal distribution of float-derived annual-average GPP, ANCP, and the export ratio. GPP estimates in (A) are
785 **euphotic zone-integrated ΔO_2-GOP quantities, converted to carbon equivalents using a photosynthetic quotient value of 1.4. ANCP**
values are from various data sources, as indicated in the figure legend or from the compilation of OSP data in section 3.1 (Fig. 5).
The black line and shading represent average ± one standard deviation values in 10° latitude bands. In (B), a float-based estimate of
the export ratio was derived by dividing average float-based ANCP by float-based NPP, using an NPP-to-GOP ratio of 2.7, as in
Johnson and Bif (2021) and Stoer and Fennel (2022). Independent estimates of the export ratio from Laws et al. (2011) and Henson
790 **et al. (2012) are also shown. The dotted black lines north of 30°S indicate poorer latitudinal representation of float-based ANCP,**
and therefore lower confidence in the derived export ratio.

Appendix A

Data handling and calculations for the OSP NCP Case Study

We compiled NCP and ANCP data from six published float/glider studies at Ocean Station Papa (OSP) in the Subarctic NE
795 Pacific (Table A1). Time-explicit NCP and ANCP values were obtained from Plant et al. (2016), Yang et al. (2017), Pelland
et al. (2018), Haskell et al. (2020) and Huang et al. (2022). We also obtained an estimate of ANCP from Bushinsky and
Emerson (2015). Yang et al. and Haskell et al. provided NCP data that were integrated to the depth of the annual maximum
mixed layer (ML), while Plant et al. and Pelland et al. provided depth-resolved estimates. Data from Huang et al. were

integrated to 56 m. We present NCP and ANCP values integrated to the annual maximum mixed layer depth (MLD), scaling

800 values from Huang et al. assuming constant NCP between 56 m and the maximum MLD.

We also obtained NCP estimates from ship-board sampling, moorings, and satellites, collected over the past two decades (Table A1). We obtained two satellite-based NCP estimates: one from a global machine learning algorithm (Li and Cassar, 2016), and the other derived as the product of satellite-NPP (average of the VGPM and CbPM models; Behrenfeld and Falkowski, 1997; Westberry et al., 2008) and a commonly used global export-ratio algorithm (e-ratio; Laws et al., 2011) (i.e.,

805 NCP = NPP x e-ratio). The ship- and mooring estimates represent NCP values integrated in the seasonal ML, while satellite-based estimates detect approximately one optical depth below the surface. Accordingly, we scaled all independent NCP estimates to the annual average maximum MLD at OSP, using MLD estimates obtained from the Argo Mixed Layers climatology (Holte et al., 2017).

We calculated ANCP as the sum of annual maximum MLD-integrated values from January through December for each full

810 year of data. We determined ship-based ANCP by integrating average monthly ML-integrated NCP values over a 12-month cycle, after linearly interpolating values between months without data. All units were converted to O_2 equivalents using a PQ value of 1.4, and O_2:NO_3^- ratio of 150:16.

Data handling and calculations for the global GPP Case Study

815 Following Stoer and Fennel (2022), we compiled all available BGC-Argo O_2 and $b_{bp,700}$ data collected between January 2010 and December 2022, selecting only the high-quality (Argo quality flags 1 and 2 representing "good" and "probably good"), "adjusted" (flag 5) and "estimated" (flag 8) O_2 data and high-quality b_{bp} data. b_{bp} profiles were de-spiked using a five-point running minimum filter followed by a five-point running maximum filter. Profile measurements were then binned into 10-m intervals from 0 to 200 m depth. We applied linear interpolation between up to two data points when data were missing. We

820 calculated ΔO_2 (mmol m^{-3}) using the corresponding float hydrographic data (Garcia and Gordon, 1993, 1992) and POC (mmol m^{-3}) following the global b_{bp}-to-POC algorithm of Graff et al. (2015), after converting $b_{bp,700}$ to $b_{bp,470}$ using a power law relationship with a slope of 0.78 (Boss and Haëntjens, 2016; Boss et al., 2013).

Treating O_2 and b_{bp} separately, we excluded a selection of floats with oceanographically inconsistent data or unrealistic O_2 and b_{bp} values (see lists in Johnson and Bif, 2021 and Stoer and Fennel, 2022). We discarded any floats that did not sample at least

825 21 unique hours of the day evenly over their life cycles. Profiles were sub-divided into different spatial groups, representing 10° latitudinal bands (70°S to 70°N) or Longhurst Biogeographical Provinces. We constructed a composite diurnal curve in each spatial subset by calculating the median ΔO_2 or b_{bp}-POC value at each hour of the day.

We performed two sets of GPP calculations only when at least 21 hours of the day were represented in each subset: 1) using all available ΔO_2 and b_{bp}-POC profiles, treating O_2 and b_{bp} independently and 2) using co-located data obtained from floats

830 containing both O_2 and b_{bp} sensors. GOP and GCP were estimated by fitting the sinusoidal GPP-vs-light function to the resulting diurnal curves. We did not consider the influence of fluxes due to air-sea exchange, vertical mixing, POC sinking or grazing on our calculated GPP estimates. We used each data subset's average location and midpoint date to determine the daily

light cycle and sunrise/sunset times. We accounted for DOC production by scaling b_{bp}-GPP estimates by a percent extracellular

release (PER) value of 0.33, calculated from the global meta-analysis of Moran et al. (2022), and converted GCP values (units

835 mmol C) to O_2 equivalents using a photosynthetic quotient of 1.4 (Laws, 1991) (i.e., $\frac{b_{bp}\text{-GCP}}{1-0.3}$ 1.4). Finally, we discarded

unrealistic GOP and GCP rates by removing values exceeding three-standard deviations of the mean of a climatological GOP

dataset (references listed in Table S1 of the SI). We did not specifically discard negative values, following the recommendation

by Barone et al. (2019), but recognize those estimates as representing undetectably-low GPP.

840

Table A1. List of data sources and archived PP datasets referenced in the manuscript.

Sources	PP type	Platform	Use in manuscript
Bushinsky & Emerson, 2015	ANCP	Float	OSP NCP case study (section 3.1, Fig. 5)
Haskell et al., 2020; Huang et al., 2022; Plant et al., 2016; Yang et al., 2017	NCP, ANCP	Float	OSP NCP case study (section 3.1, Fig. 5)
Pelland et al., 2018	NCP, ANCP	Glider	OSP NCP case study (section 3.1, Fig. 5)
Li & Cassar, 2016	NCP	Satellite	OSP NCP case study (section 3.1, Fig. 5)
Emerson, 2014; Emerson & Stump, 2010; Fassbender et al., 2016	ANCP, NCP	Mooring	Archived PP map (Fig. 1) OSP NCP case study (section 3.1, Fig. 5)
Giesbrecht et al., 2012; Hamme et al., 2010; Howard et al., 2010; Izett et al., 2018, 2021; Juranek et al., 2012; Kavanaugh et al., 2014; Lockwood et al., 2012; Palevsky et al., 2016; Timmerman & Hamme, 2021	NCP	Ship	Archived PP map (Fig. 1) OSP NCP case study (section 3.1, Fig. 5)
Cynar et al., 2021; Hamme et al., 2012; Izett & Tortell, 2021; L. Juranek, 2020; Li & Cassar, 2016*; Ouyang et al., 2021; Qin et al., 2021, 2021; Seguro et al., 2019; Wang et al., 2020	NCP	Ship	Archived PP map (Fig. 1)
Johnson, 2010; Körtzinger et al., 2008; Weeding & Trull, 2014	NCP, ANCP	Mooring	Archived PP map (Fig. 1)
Alkire et al., 2012; Baetge et al., 2020; Huang et al., 2018; Yang, 2021; Emerson and Yang, 2022; Yang et al., 2019	NCP	Float	Archived PP map (Fig. 1)
Alkire et al., 2014; Binetti et al., 2020; Haskell et al., 2019; Hull et al., 2021; Possenti et al., 2021	NCP	Glider	Archived PP map (Fig. 1)
Barbieux et al., 2022; Briggs et al., 2018; Gordon et al., 2020; Henderikx Freitas et al., 2020; Johnson & Bif, 2021	GPP	Float	Archived PP map (Fig. 1)
Barone et al., 2019; Nicholson et al., 2015	GPP	Glider	Archived PP map (Fig. 1)
Huang et al., 2021*	GPP	Ship	Archived PP map (Fig. 1) Global GPP case study (section 3.2, Fig. 6)

OSP = Ocean Station Papa; *Data compiled by Li & Cassar (2016) and Huang et al. (2021).

845 **Table A2 Summary of published float-based GPP and NCP studies. (g) denotes glider-based studies.**

Method	Variables	PP fraction	Reference
Diurnal	O_2	GPP	Barone et al., 2019 (g); Briggs et al., 2018; Gordon et al., 2020; Henderikx Freitas et al., 2020; Nicholson et al., 2015 (g)
Diurnal	POC	GPP	Barbieux et al., 2022; Briggs et al., 2018
Diurnal	O_2 (composite)	GPP, NPP	Johnson and Bif, 2021; Stoer and Fennel, 2022
Diurnal	POC (composite)	GPP, NPP	Stoer and Fennel, 2022
Budget	O_2	NCP, ANCP	Alkire et al., 2012, 2014 (g); Binetti et al., 2020 (g); Bushinsky and Emerson, 2015; Haskell et al., 2019 (g); Huang et al., 2018, 2022; Pelland et al., 2018 (g); Plant et al., 2016; Possenti et al., 2021 (g); Yang, 2021; Yang et al., 2017, 2018, 2019; Emerson and Yang, 2022.
Budget	NO_3^-	NCP, ANCP	Haskell et al., 2020; Huang et al., 2022; Plant et al., 2016
Budget	POC, TA, DIC	NCP, ANCP	Huang et al., 2022
Seasonal change	O_2, NO_3^-, DIC	NCP	Baetge et al., 2020; Hull et al., 2021 (g); Johnson et al., 2017

Table A3 Variations in budget terms used in float- and glider-based NCP calculations.

Study	Platform	T	Vertical resolution	$F_{AS} + F_{EP}$ (surface only)	κ_z [m² s⁻¹]	w [m s⁻¹]	dh/dt [m d⁻¹]	u + v [m d⁻¹]
Alkire et al. 2012	Float	O_2	1 box (0-27.3 kg m⁻³)	$F_{AS} = k_{O2} (O_2 - O_{2,eq}[1+\Delta_{eq}])$	0	0	0	0
Alkire et al., 2014	Glider	O_2	1 box (0-27.3 kg m⁻³)	Δ_{eq} (Woolfe & Thorpe, 1991) k_{O2} (Wanninkhof, 1992) $F_{AS} = k_{O2} (O_2 - O_{2,eq}[1+\Delta_{eq}])$	10⁻⁴	0	0	estimated from glider displacement between profiles NCEP/NCAR reanalysis
Bushinsky & Emerson, 2015*	Float	O_2	N box (0-MLD; MLD-150 m; $\Delta h = 1.5$ m)	Δ_{eq} (Woolfe & Thorpe, 1991) k_{O2} (Wanninkhof, 1992) $F_{AS} = k_{O2} (O_2-O_{2,eq}) + \beta(F_c+F_p)$; $\beta=1$, 0.29	Cronin et al. (2015) (surface); Sun et al. (2013) (profile)	Ekman pumping velocity	derived from observations; > 0 only	0
Plant et al., 2016*	Float	O_2, NO_3^-	N box (0-180 m; $\Delta h = 2$ m)	$F_{AS}=k_{O2} (O_2-O_{2,eq}) + (F_{bub.})$ (Liang et al., 2013, scaled to NO_3^- ANCP)	1.5x10⁻⁵	PWP	PWP	0
Yang et al., 2017*; 2018; 2019; 2021; Yang 2021	Float	O_2	2 box (0-MLD; MLD-max. MLD)	$F_{AS} = k_{O2} (O_2-O_{2,eq}) + \beta(F_c+F_p)$; $\beta = 1$, 0.53 (Liang et al., 2013)	1.5x10⁻⁵ (box 2 only)	0	derived from observations; > 0 only	0
Huang et al., 2018	Float	O_2	2 box (0-MLD; MLD-max. MLD)	$F_{AS} = k_{O2} (O_2-O_{2,eq}) + (F_c+F_p)$ (Liang et al., 2013)	10⁻⁵ m² s⁻¹ (box 2 only)	0	derived from observations; > 0 only	0
Pelland et al., 2018*	Glider	O_2	86 boxes (0-150 m, $\Delta h = 2$ m; 150-200 m, $\Delta h = 5$m)	$F_{AS} = k_{O2} (O_2-O_{2,eq}) + \beta(F_c+F_p)$; $\beta = 0.29$ (Liang et al., 2013)	T/S budget	T/S budget	0	T/S budget
Haskell et al., 2019	Glider	O_2	2 box (0-MLD, MLD-EuZ)	$F_{AS} = k_{O2} (O_{2,eq})$ $(\Delta O_2/Ar)$ k_{O2} (Nightingale et al., 2000)	Haskell et al., 2016	Bakun upwelling index	0	0

850 **Table A3 Continued.**

Study	Platform	T	Vertical resolution	$F_{AS} + F_{EP}$ (surface only)	κ_Z [m² s⁻¹]	w [m s⁻¹]	dh/dt [m d⁻¹]	u + v [m d⁻¹]
Binetti et al., 2020	Glider	O_2	1 box (0-60m)	$F_{AS} = k_{O2} (O_2 - O_{2,eq}[1+\Delta_{eq}])$ Δ_{eq} (Woolfe & Thorpe, 1991) k_{O2} (Nightingale et al., 2000)	0	0	derived from observations; > 0 only	0
Haskell et al., 2020*	Float	NO_3^-	1 box (0-Z, where Z = MLD, EuZ, 100 m or max. MLD)	$F_{EP}=(dS/dt - dS/dt_{phys})$ (T:S)	Cronin et al., (2015), scaled to DIC budget	Ekman pumping velocity	derived from observations; > 0 only	0
Possenti et al., 2021	Glider	O_2	1 box (0-45 m)	$F_{AS} = k_{O2} (O_2 - O_{2,eq}[1+\Delta_{eq}])$ Δ_{eq} (Woolfe & Thorpe, 1991) k_{O2} (Wanninkhof, 1992)	10^{-5}	0	derived from observations; > 0 only	0
Huang et al., 2022*	Float	O_2, NO_3^-, POC, TIC, TA	1 box (0-56 m)	$F_{EP}= k_{CO2} (k_H) (\Delta pCO_2) + (dS/dt-dS/dt_{phys})$ (C:S) $F_{AS}=k_{CO2} (O_2-O_{2,eq}) + (F_{bub.})$	Cronin et al. (2015) (surface); Sun et al. (2013) (profile)	Ekman pumping velocity	derived from observations; > 0 & MLD > 56 m, otherwise 0	0
Hull et al.,2022	Float	O_2, NO_3^-	1 box (0-EUZ)	k_{CO2} (Wanninkhof, 2014) $F_{AS,O2}$ (Liang et al., 2013) $F_{AS} = k_{O2} (O_2 - O_{2,eq}[1+\Delta_{eq}])$ Δ_{eq} (Liang et al., 2013) k_{O2} (Nightingale et al., 2000)	0	0	0	0

* = Studies at OSP; F_{AS} = air-sea gas exchange (mol m⁻² d⁻¹); F_{AS} = air-sea bubble flux (mol m⁻² d⁻¹); F_{EP} = evaporation or precipitation (mol m⁻² d⁻¹); κ_Z = eddy diffusivity coefficient [m² d⁻¹]; w = vertical advection velocity [m d⁻¹]; dh/dt = change in layer depth [m d⁻¹]; u + v = horizontal advection velocities [m d⁻¹]; Δh = box vertical displacement (h_{i+1} – h_i in Eq. 7); C:S = observed DIC:salinity ratio [mol C:S].

β = bubble-mediated transfer scaling coefficient [unitless]; PWP = Price-Weller-Pinkel mixed layer model (Price et al., 1986); C:S = observed DIC:salinity ratio [mol C:S].

Code and Data Availability

855   The GPP data in our global case study analysis were derived by modifying the code provided by Stoer and Fennel (2022) at doi.org/10.5281/zenodo.6977161. The code was only modified to perform GPP calculations in the geographic regions (10º latitude bands and Longhurst Biogeographic Provinces) described in the main text. Shape files for the Longhurst Biogeographic Province boundaries are available from https://www.marineregions.org/sources.php#longhurst (Flanders Marine Institute, 2009). NCP data from our OSP case study analysis is available at doi.org/10.5281/zenodo.7667521.

860   Additional GPP and NCP data included in this manuscript were compiled from the publications listed in Table A1 of the appendix. BGC-Argo data were collected and made freely available by the International Argo Program and the national programs that contribute to it (Argo, 2023). The Argo Program is part of the Global Ocean Observing System. Float data are available from the Argo Global Data Assembly Centers in Brest, France (ftp://ftp.ifremer.fr/ifremer/argo/dac/coriolis) and Monterey, USA (ftp://usgodae.org/pub/outgoing/argo/dac/coriolis).

865   **Author contributions**

All authors contributed to the planning and preparation of the manuscript. RWI wrote the manuscript, with significant contributions and feedback from all authors. ACS performed the global GPP calculations. RWI compiled the OSP NCP data and performed all analyses on the GPP and NCP data.

Competing interests

870   The authors declare that they have no conflict of interest.

Acknowledgements

We would like to thank the BGC-Argo community for supporting the float array through funding acquisitions, deployments, and data management, and for making the resulting data freely available. We also thank many colleagues for making their processed data available for analysis in this paper. In particular, we thank A. Fassbender, W. Haskell, Y. Huang, N. Pelland,

875   J. Plant and B. Yang for their assistance. This work was supported by the Ocean Frontier Institute (OFI) and Canada First Research Excellence Fund (CFREF) through an International Postdoctoral Fellowship to RWI. KF received support from the Natural Sciences and Engineering Research Council of Canada (NSERC) through a Discovery Grant (RGPIN-2014-03938). AS was supported by a Nova Scotia Graduate Student scholarship and by NSERC through a Canada Graduate Scholarship. DN was supported by the National Science Foundation's (NSF) Global Ocean Biogeochemistry Array (GO-BGC) Project

880   under the NSF Award 1946578 with operational support from NSF Award 2110258, as well as support from NSF OCE#
2023080.

References

Ainsworth, C. H., Samhouri, J. F., Busch, D. S., Cheung, W. W. L., Dunne, J., and Okey, T. A.: Potential impacts of climate change on Northeast Pacific marine foodwebs and fisheries, ICES Journal of Marine Science, 68, 1217–1229,
885   https://doi.org/10.1093/icesjms/fsr043, 2011.

Alkire, M. B., D'Asaro, E., Lee, C., Jane Perry, M., Gray, A., Cetinić, I., Briggs, N., Rehm, E., Kallin, E., Kaiser, J., and González-Posada, A.: Estimates of net community production and export using high-resolution, Lagrangian measurements of O2, NO3−, and POC through the evolution of a spring diatom bloom in the North Atlantic, Deep Sea Research Part I: Oceanographic Research Papers, 64, 157–174, https://doi.org/10.1016/j.dsr.2012.01.012, 2012.

890   Alkire, M. B., Lee, C., D'Asaro, E., Perry, M. J., Briggs, N., Cetinić, I., and Gray, A.: Net community production and export from Seaglider measurements in the North Atlantic after the spring bloom, Journal of Geophysical Research: Oceans, 119, 6121–6139, https://doi.org/10.1002/2014JC010105, 2014.

Argo: Argo float data and metadata from Global Data Assembly Centre (Argo GDAC). SEANOE, https://doi.org/10.17882/42182, 2023.

895   Atamanchuk, D., Koelling, J., Send, U., and Wallace, D. W. R.: Rapid transfer of oxygen to the deep ocean mediated by bubbles, Nature Geoscience, 13, 232–237, https://doi.org/10.1038/s41561-020-0532-2, 2020.

Baetge, N., Graff, J. R., Behrenfeld, M. J., and Carlson, C. A.: Net Community Production, Dissolved Organic Carbon Accumulation, and Vertical Export in the Western North Atlantic, Frontiers in Marine Science, 7, 1–16, https://doi.org/10.3389/fmars.2020.00227, 2020.

900   Baines, S. B. and Pace, M. L.: The production of dissolved organic matter by phytoplankton and its importance to bacteria: Patterns across marine and freshwater systems, Limnology and Oceanography, 36, 1078–1090, https://doi.org/10.4319/lo.1991.36.6.1078, 1991.

Barbieux, M., Uitz, J., Mignot, A., Roesler, C., Claustre, H., Gentili, B., Taillandier, V., D'Ortenzio, F., Loisel, H., Poteau, A., Leymarie, E., Penkerc'h, C., Schmechtig, C., and Bricaud, A.: Biological production in two contrasted regions of the
905   Mediterranean Sea during the oligotrophic period: an estimate based on the diel cycle of optical properties measured by BioGeoChemical-Argo profiling floats, Biogeosciences, 19, 1165–1194, https://doi.org/10.5194/bg-19-1165-2022, 2022.

Barone, B., Nicholson, D., Ferrón, S., Firing, E., and Karl, D.: The estimation of gross oxygen production and community respiration from autonomous time-series measurements in the oligotrophic ocean, Limnology and Oceanography: Methods, 17, 650–664, https://doi.org/10.1002/lom3.10340, 2019.

910   Behrenfeld, M. J. and Falkowski, P. G.: Photosynthetic rates derived from satellite-based chlorophyll concentration, Limnology and Oceanography, 42, 1–20, https://doi.org/10.4319/lo.1997.42.1.0001, 1997.

Bender, M., Grande, K., Johnson, K., Marra, J., Williams, P. J. L. B., Sieburth, J., Pilson, M., Langdon, C., Hitchcock, G., Orchardo, J., Hunt, C., Donaghay, P., and Heinemann, K.: A comparison of four methods for determining planktonic community production, Limnology and Oceanography, 32, 1085–1098, https://doi.org/10.4319/lo.1987.32.5.1085, 1987.

915 Bender, M. L., Kinter, S., Cassar, N., and Wanninkhof, R.: Evaluating gas transfer velocity parameterizations using upper ocean radon distributions, Journal of Geophysical Research, 116, 1–11, https://doi.org/10.1029/2009JC005805, 2011.

Bif, M. B. and Hansell, D. A.: Seasonality of Dissolved Organic Carbon in the Upper Northeast Pacific Ocean, Global Biogeochemical Cycles, 33, 526–539, https://doi.org/10.1029/2018GB006152, 2019.

Binetti, U., Kaiser, J., Damerell, G. M., Rumyantseva, A., Martin, A. P., Henson, S., and Heywood, K. J.: Net community
920 oxygen production derived from Seaglider deployments at the Porcupine Abyssal Plain site (PAP; northeast Atlantic) in 2012–13, Progress in Oceanography, 183, 102293, https://doi.org/10.1016/j.pocean.2020.102293, 2020.

Biogeochemical-Argo Planning Group.: The Scientific rationale, design and Implementation Plan for a Biogeochemical-Argo float array, 2016.

Bittig, H. C., Steinhoff, T., Claustre, H., Fiedler, B., Williams, N. L., Sauzède, R., Körtzinger, A., and Gattuso, J.-P.: An
925 Alternative to Static Climatologies: Robust Estimation of Open Ocean CO2 Variables and Nutrient Concentrations From T, S, and O2 Data Using Bayesian Neural Networks, Frontiers in Marine Science, 5, 2018.

Bol, R., Henson, S. A., Rumyantseva, A., and Briggs, N.: High-Frequency Variability of Small-Particle Carbon Export Flux in the Northeast Atlantic, Global Biogeochemical Cycles, 32, 1803–1814, https://doi.org/10.1029/2018GB005963, 2018.

Bopp, L., Resplandy, L., Orr, J. C., Doney, S. C., Dunne, J. P., Gehlen, M., Halloran, P., Heinze, C., Ilyina, T., Séférian, R.,
930 Tjiputra, J., and Vichi, M.: Multiple stressors of ocean ecosystems in the 21st century: projections with CMIP5 models, Biogeosciences, 10, 6225–6245, https://doi.org/10.5194/bg-10-6225-2013, 2013.

Boss, E., Picheral, M., Leeuw, T., Chase, A., Karsenti, E., Gorsky, G., Taylor, L., Slade, W., Ras, J., and Claustre, H.: The characteristics of particulate absorption, scattering and attenuation coefficients in the surface ocean; Contribution of the Tara Oceans expedition, Methods in Oceanography, 7, 52–62, https://doi.org/10.1016/j.mio.2013.11.002, 2013.

935 Boss, E. B. and Haëntjens, N.: Primer regarding measurements of chlorophyll fluorescence and the backscattering coefficient with WETLabs FLBB on profiling floats., SOCCOM, Princeton University, https://doi.org/10.25607/OBP-50, 2016.

Briggs, N., Guemundsson, K., Cetinić, I., D'Asaro, E., Rehm, E., Lee, C., and Perry, M. J.: A multi-method autonomous assessment of primary productivity and export efficiency in the springtime North Atlantic, Biogeosciences, 15, 4515–4532, https://doi.org/10.5194/bg-15-4515-2018, 2018.

940 Burt, W. J., Westberry, T. K., Behrenfeld, M. J., Zeng, C., Izett, R. W., and Tortell, P. D.: Carbon : Chlorophyll ratios and net primary productivity of Subarctic Pacific surface waters derived from autonomous shipboard sensors, Global Biogeochemical Cycles, 32, 267–288, https://doi.org/10.1002/2017GB005783, 2018.

Bushinsky, S. M. and Emerson, S.: Marine biological production from in situ oxygen measurements on a profiling float in the subarctic Pacific Ocean, Global Biogeochemical Cycles, 29, 2050–2060, https://doi.org/10.1002/2015GB005251, 2015.

945 Carter, B. R., Bittig, H. C., Fassbender, A. J., Sharp, J. D., Takeshita, Y., Xu, Y.-Y., Álvarez, M., Wanninkhof, R., Feely, R. A., and Barbero, L.: New and updated global empirical seawater property estimation routines, Limnology and Oceanography: Methods, 19, 785–809, https://doi.org/10.1002/lom3.10461, 2021.

Cetinić, I., Perry, M. J., Briggs, N. T., Kallin, E., D'Asaro, E. A., and Lee, C. M.: Particulate organic carbon and inherent optical properties during 2008 North Atlantic Bloom Experiment, Journal of Geophysical Research: Oceans, 117,
950 https://doi.org/10.1029/2011JC007771, 2012.

Chai, F., Johnson, K. S., Claustre, H., Xing, X., Wang, Y., Boss, E., Riser, S., Fennel, K., Schofield, O., and Sutton, A.: Monitoring ocean biogeochemistry with autonomous platforms, Nature Reviews Earth and Environment, 1, 315–326, https://doi.org/10.1038/s43017-020-0053-y, 2020.

Claustre, H., Huot, Y., Obernosterer, I., Gentili, B., Tailliez, D., and Lewis, M.: Gross community production and metabolic
955 balance in the South Pacific Gyre, using a non intrusive bio-optical method, Biogeosciences, 5, 463–474, https://doi.org/10.5194/bg-5-463-2008, 2008.

Cronin, M. F., Pellan, N. A., Emerson, S. R., and Crawford, W. R.: Estimating diffusivity from the mixed layer heat and salt balances in the North Pacific, Journal of Geophysical Research: Oceans, 120, 7346–7362, https://doi.org/10.1002/2015JC011010, 2015.

960 Cullen, J. J.: Primary Production Methods, in: Encyclopedia of Ocean Sciences, Elsevier, 2277–2284, https://doi.org/10.1006/rwos.2001.0203, 2001.

Cynar, H., Juranek, L. W., Mordy, C., Strausz, D., and Bell, S.: Underway O2/Ar (Oxygen/Argon) and oxygen data collected on a research cruise on the vessel Ocean Starr, Bering, Chukchi, and Beaufort Seas, Arctic Ocean, 2019., https://doi.org/10.18739/A2HH6C69V, 2021.

965 Emerson, S.: Annual net community production and the biological carbon flux in the ocean, Global Biogeochemical Cycles, 14–28, https://doi.org/10.1002/2013GB004680, 2014.

Emerson, S. and Bushinsky, S.: The role of bubbles during air-sea gas exchange, Journal of Geophysical Research: Oceans, 121, 4360–4376, https://doi.org/10.1002/2016JC011744, 2016.

Emerson, S. and Stump, C.: Net biological oxygen production in the ocean-II: Remote in situ measurements of O_2 and N_2 in
970 subarctic pacific surface waters, Deep-Sea Research Part I, 57, 1255–1265, https://doi.org/10.1016/j.dsr.2010.06.001, 2010.

Emerson, S. and Yang, B.: The Ocean's Biological Pump: In Situ Oxygen Measurements in the Subtropical Oceans, Geophysical Research Letters, 49, e2022GL099834, https://doi.org/10.1029/2022GL099834, 2022.

Emerson, S., Yang, B., White, M., and Cronin, M.: Air-Sea Gas Transfer : Determining Bubble Fluxes with In Situ N 2 Observations, Journal of Geophysical Research: Oceans, Accepted, https://doi.org/10.1029/2018JC014786, 2019.

975 Fassbender, A. J., Sabine, C. L., and Cronin, M. F.: Net community production and calcification from 7 years of NOAA Station Papa Mooring measurements, Global Biogeochemical Cycles, 30, 250–267, https://doi.org/10.1002/2015GB005205, 2016.

Ferrón, S., del Valle, D. A., Björkman, K. M., Quay, P. D., Church, M. J., and Karl, D. M.: Application of membrane inlet mass spectrometry to measure aquatic gross primary production by the 18O in vitro method, Limnology and Oceanography: Methods, 14, 610–622, https://doi.org/10.1002/lom3.10116, 2016.

980 Flanders Marine Institute: Longhurst Provinces. Available online at https://www.marineregions.org. Accessed Dec. 2021., 2009.

Gaarder, T. and Gran, H., H.: Investigations of the Production of Phytoplankton in the Oslo Fjord, Rapports et procès-verbaux des réunions/Conseil international pour l'exploration de la mer, 42, 1–48, 1927.

Garcia, H. E. and Gordon, L. I.: Oxygen solubility in Seawater: better fitting equations, Limnology and Oceanography, 37,
985 1307–1312, https://doi.org/10.2307/2837876, 1992.

Garcia, H. E. and Gordon, L. I.: Erratum: Oxygen solubility in seawater: better fitting equations, Limnology and Oceanography, 38, 656, 1993.

Gattuso, J.-P., Epitalon, J.-M., Lavigne, H., Orr, J., Gentili, B., Hagens, M., Hofmann, A., Mueller, J.-D., Proye, A., Rae, J., and Soetaert, K.: seacarb: Seawater Carbonate Chemistry, 2022.

990 Giesbrecht, K. E., Hamme, R. C., and Emerson, S. R.: Biological productivity along Line P in the subarctic northeast Pacific: In situ versus incubation-based methods, Global Biogeochemical Cycles, 26, https://doi.org/10.1029/2012GB004349, 2012.

Gordon, C., Fennel, K., Richards, C., Shay, L. K., and Brewster, J. K.: Can ocean community production and respiration be determined by measuring high-frequency oxygen profiles from autonomous floats?, Biogeosciences, 17, 4119–4134, https://doi.org/10.5194/bg-17-4119-2020, 2020.

995 Gordon, H. R. and McCluney, W. R.: Estimation of the Depth of Sunlight Penetration in the Sea for Remote Sensing, Appl. Opt., AO, 14, 413–416, https://doi.org/10.1364/AO.14.000413, 1975.

Graff, J. R., Westberry, T. K., Milligan, A. J., Brown, M. B., Dall'Olmo, G., Dongen-Vogels, V. van, Reifel, K. M., and Behrenfeld, M. J.: Analytical phytoplankton carbon measurements spanning diverse ecosystems, Deep Sea Research Part I: Oceanographic Research Papers, 102, 16–25, https://doi.org/10.1016/j.dsr.2015.04.006, 2015.

1000 Hamme, R. C., Webley, P. W., Crawford, W. R., Whitney, F. A., Degrandpre, M. D., Emerson, S. R., Eriksen, C. C., Giesbrecht, K. E., Gower, J. F. R., Kavanaugh, M. T., Pena, M. A., Sabine, C. L., Batten, S. D., Coogan, L. A., Grundle, D. S., and Lockwood, D.: Volcanic ash fuels anomalous plankton bloom in subarctic northeast Pacific, Geophysical Research Letters, 37, https://doi.org/10.1029/2010GL044629, 2010.

Hamme, R. C., Cassar, N., Lance, V. P., Vaillancourt, R. D., Bender, M. L., Strutton, P. G., Moore, T. S., DeGrandpre, M. D., 1005 Sabine, C. L., Ho, D. T., and Hargreaves, B. R.: Dissolved O2/Ar and other methods reveal rapid changes in productivity during a Lagrangian experiment in the Southern Ocean, Journal of Geophysical Research: Oceans, 117, 1–19, https://doi.org/10.1029/2011JC007046, 2012.

Haskell, W. Z., Hammond, D. E., Prokopenko, M. G., Teel, E. N., Seegers, B. N., Ragan, M. A., Rollins, N., and Jones, B. H.: Net Community Production in a Productive Coastal Ocean From an Autonomous Buoyancy-Driven Glider, Journal of 1010 Geophysical Research: Oceans, 4188–4207, https://doi.org/10.1029/2019JC015048, 2019.

Haskell, W. Z., Fassbender, A. J., Long, J. S., and Plant, J. N.: Annual Net Community Production of Particulate and Dissolved Organic Carbon From a Decade of Biogeochemical Profiling Float Observations in the Northeast Pacific, Global Biogeochemical Cycles, 34, 1–22, https://doi.org/10.1029/2020GB006599, 2020.

Henderikx Freitas, F., White, A. E., and Quay, P. D.: Diel Measurements of Oxygen- and Carbon-Based Ocean Metabolism 1015 Across a Trophic Gradient in the North Pacific, Global Biogeochemical Cycles, 34, https://doi.org/10.1029/2019gb006518, 2020.

Henderikx-Freitas, F., Allen, J. G., Lansdorp, B. M., and White, A. E.: Diel variations in the estimated refractive index of bulk oceanic particles, Opt. Express, OE, 30, 44141–44159, https://doi.org/10.1364/OE.469565, 2022.

Henson, S. A., Sanders, R., and Madsen, E.: Global patterns in efficiency of particulate organic carbon export and transfer to 1020 the deep ocean, Global Biogeochemical Cycles, 26, https://doi.org/10.1029/2011GB004099, 2012.

Hoegh-Guldberg, O. and Bruno, J.: The Impact of Climate Change on the World's Marine Ecosystems, Science, 328, 1523–1528, https://doi.org/10.1126/science.1189930, 2010.

Holte, J., Talley, L. D., Gilson, J., and Roemmich, D.: An Argo mixed layer climatology and database, Geophysical Research Letters, 44, 5618–5626, https://doi.org/10.1002/2017GL073426, 2017.

1025   Howard, E., Emerson, S., Bushinsky, S., and Stump, C.: The role of net community production in air-sea carbon fluxes at the North Pacific subarctic-subtropical boundary region, Limnology and Oceanography, 55, 2585–2596, https://doi.org/10.4319/lo.2010.55.6.2585, 2010.

Huang, Y., Yang, B., Chen, B., Qiu, G., Wang, H., and Huang, B.: Net community production in the South China Sea Basin estimated from in situ O2 measurements on an Argo profiling float, Deep Sea Research Part I: Oceanographic Research Papers, 1030   131, 54–61, https://doi.org/10.1016/j.dsr.2017.11.002, 2018.

Huang, Y., Nicholson, D., Huang, B., and Cassar, N.: Global Estimates of Marine Gross Primary Production Based on Machine Learning Upscaling of Field Observations, Global Biogeochemical Cycles, 35, 1–18, https://doi.org/10.1029/2020GB006718, 2021.

Huang, Y., Fassbender, A. J., Long, J. S., Johannessen, S., and Bernardi Bif, M.: Partitioning the Export of Distinct Biogenic 1035   Carbon Pools in the Northeast Pacific Ocean Using a Biogeochemical Profiling Float, Global Biogeochemical Cycles, 36, https://doi.org/10.1029/2021gb007178, 2022.

Hull, T., Greenwood, N., Birchill, A., Beaton, A., Palmer, M., and Kaiser, J.: Simultaneous assessment of oxygen and nitrate-based net community production in a temperate shelf sea from a single ocean glider, Biogeosciences Discussions, 1–25, https://doi.org/10.5194/bg-2021-170, 2021.

1040   Izett, R. W. and Tortell, P.: High-resolution, mixed layer NCP estimates and ancillary data from the Central and Eastern North American Arctic: 2015, 2018, 2019 (Dataset), , https://doi.org/10.5281/zenodo.5593381, 2021.

Izett, R. W., Manning, C. C., Hamme, R. C., and Tortell, P. D.: Refined Estimates of Net Community Production in the Subarctic Northeast Pacific Derived From ΔO_2/Ar Measurements With N_2O-Based Corrections for Vertical Mixing, Global Biogeochemical Cycles, 32, 326–350, https://doi.org/10.1002/2017GB005792, 2018.

1045   Izett, R. W., Schuler, K., and Tortell, P.: Underway surface O2/Ar, O2 and N2 observations from the Subarctic Northeast Pacific (Dataset), , https://doi.org/10.1594/PANGAEA.933345, 2021.

Johnson, K., Coletti, L., and Chavez, F.: Diel nitrate cycles observed with in situ sensors predict monthly and annual new production, Deep Sea Research Part I: Oceanographic Research Papers, 53, 561–573, https://doi.org/10.1016/j.dsr.2005.12.004, 2006.

1050   Johnson, K. S.: Simultaneous measurements of nitrate, oxygen, and carbon dioxide on oceanographic moorings: Observing the Redfield ratio in real time, Limnology and Oceanography, 55, 615–627, https://doi.org/10.4319/lo.2009.55.2.0615, 2010.

Johnson, K. S. and Bif, M. B.: Constraint on net primary productivity of the global ocean by Argo oxygen measurements, Nature Geoscience, 14, 769–774, https://doi.org/10.1038/s41561-021-00807-z, 2021.

Johnson, K. S., Plant, J. N., Dunne, J. P., Talley, L. D., and Sarmiento, J. L.: Annual nitrate drawdown observed by SOCCOM 1055   profiling floats and the relationship to annual net community production, Journal of Geophysical Research: Oceans, 122, 6668–6683, https://doi.org/10.1002/2017JC012839, 2017.

Juranek, L. W.: KM1906_Gradients3_Surface_O2Ar_NCP, https://doi.org/10.5281/zenodo.4009653, 2020.

Juranek, L. W., Quay, P. D., Feely, R. A., Lockwood, D., Karl, D. M., and Church, M. J.: Biological production in the NE Pacific and its influence on air-sea CO 2 flux: Evidence from dissolved oxygen isotopes and O 2 /Ar, Journal of Geophysical Research: Oceans, 117, n/a-n/a, https://doi.org/10.1029/2011JC007450, 2012.

Kaiser, J., Reuer, M. K., Barnett, B., and Bender, M. L.: Marine productivity estimates from continuous O2/Ar ratio measurements by membrane inlet mass spectrometry, Geophysical Research Letters, 32, 1–5, https://doi.org/10.1029/2005GL023459, 2005.

Kavanaugh, M. T., Emerson, S. R., Hales, B., Lockwood, D. M., Quay, P. D., and Letelier, R. M.: Physicochemical and biological controls on primary and net community production across northeast Pacific seascapes, Limnology and Oceanography, 59, 2013–2027, https://doi.org/10.4319/lo.2014.59.6.2013, 2014.

Körtzinger, A., Send, U., Wallace, D. W. R., Karstensen, J., and de Grandpre, M.: Seasonal cycle of O2 and pCO2 in the central Labrador Sea: Atmospheric, biological, and physical implications, Global Biogeochemical Cycles, 22, 1–16, https://doi.org/10.1029/2007GB003029, 2008.

Laws, E. A.: Photosynthetic quotients, new production and net community production in the open ocean, Deep Sea Research, 38, 143–167, 1991.

Laws, E. A., D'Sa, E., and Naik, P.: Simple equations to estimate ratios of new or export production to total production from satellite-derived estimates of sea surface temperature and primary production, Limnology and Oceanography: Methods, 9, 593–601, https://doi.org/10.4319/lom.2011.9.593, 2011.

Li, Z. and Cassar, N.: Satellite estimates of net community production based on O2/Ar observations and comparison to other estimates, Global Biogeochemical Cycles, 30, https://doi.org/10.1002/2015GB005314, 2016.

Liang, J. H., Deutsch, C., McWilliams, J. C., Baschek, B., Sullivan, P. P., and Chiba, D.: Parameterizing bubble-mediated air-sea gas exchange and its effect on ocean ventilation, Global Biogeochemical Cycles, 27, 894–905, https://doi.org/10.1002/gbc.20080, 2013.

Lockwood, D., Quay, P. D., Kavanaugh, M. T., Juranek, L. W., and Feely, R. A.: High-resolution estimates of net community production and air-sea CO 2 flux in the northeast Pacific, Global Biogeochemical Cycles, 26, 2012GB004380, https://doi.org/10.1029/2012GB004380, 2012.

Loisel, H., Vantrepotte, V., Norkvist, K., Mériaux, X., Kheireddine, M., Ras, J., Pujo-Pay, M., Combet, Y., Leblanc, K., Dall'Olmo, G., Mauriac, R., Dessailly, D., and Moutin, T.: Characterization of the bio-optical anomaly and diurnal variability of particulate matter, as seen from scattering and backscattering coefficients, in ultra-oligotrophic eddies of the Mediterranean Sea, Biogeosciences, 8, 3295–3317, https://doi.org/10.5194/bg-8-3295-2011, 2011.

Long, J. S., Fassbender, A. J., and Estapa, M. L.: Depth-Resolved Net Primary Production in the Northeast Pacific Ocean: A Comparison of Satellite and Profiling Float Estimates in the Context of Two Marine Heatwaves, Geophysical Research Letters, 48, 1–11, https://doi.org/10.1029/2021GL093462, 2021.

Longhurst, A., R.: Ecological Geography of the Sea, 2nd Edition., Academic Press, San Diego, 2006.

Luz, B. and Barkan, E.: Assessment of Oceanic Productivity with the Triple-Isotope Composition of Dissolved Oxygen, Science, 288, 2028–2031, https://doi.org/10.1126/science.288.5473.2028, 2000.

Martinez-Vicente, V., Tilstone, G. H., Sathyendranath, S., Miller, P. I., and Groom, S. B.: Contributions of phytoplankton and bacteria to the optical backscattering coefficient over the Mid-Atlantic Ridge, Marine Ecology Progress Series, 445, 37–51, https://doi.org/10.3354/meps09388, 2012.

Moran, M. A., Ferrer-González, F. X., Fu, H., Nowinski, B., Olofsson, M., Powers, M. A., Schreier, J. E., Schroer, W. F., Smith, C. B., and Uchimiya, M.: The Ocean's labile DOC supply chain, Limnology and Oceanography, 67, 1007–1021, https://doi.org/10.1002/lno.12053, 2022.

Nicholson, D. P., Wilson, S. T., Doney, S. C., and Karl, D. M.: Quantifying subtropical North Pacific gyre mixed layer primary productivity from Seaglider observations of diel oxygen cycles, Geophysical Research Letters, 42, 4032–4039, https://doi.org/10.1002/2015GL063065, 2015.

Ouyang, Z., Qi, D., Zhong, W., Chen, L., Gao, Z., Lin, H., Sun, H., Li, T., and Cai, W.-J.: Summertime Evolution of Net Community Production and CO2 Flux in the Western Arctic Ocean, Global Biogeochemical Cycles, 35, e2020GB006651, https://doi.org/10.1029/2020GB006651, 2021.

Palevsky, H. I., Quay, P. D., Lockwood, D. E., and Nicholson, D. P.: The annual cycle of gross primary production, net community production, and export efficiency across the North Pacific Ocean, Global Biogeochemical Cycles, 30, 361–380, https://doi.org/10.1002/2015GB005318, 2016.

Pei, S. and Laws, E. A.: Does the 14C method estimate net photosynthesis? Implications from batch and continuous culture studies of marine phytoplankton, Deep Sea Research I, 82, 1–9, https://doi.org/10.1016/j.dsr.2013.07.011, 2013.

Pelland, N. A., Eriksen, C. C., Emerson, S. R., and Cronin, M. F.: Seaglider Surveys at Ocean Station Papa: Oxygen Kinematics and Upper-Ocean Metabolism, Journal of Geophysical Research: Oceans, 123, 6408–6427, https://doi.org/10.1029/2018JC014091, 2018.

Plant, J. N., Johnson, K. S., Sakamoto, C. M., Jannasch, H. W., Coletti, L. J., Riser, S. C., and Swift, D. D.: Net community production at Ocean Station Papa observed with nitrate and oxygen sensors on profiling floats, Global Biogeochemical Cycles, 30, 859–879, https://doi.org/10.1002/2015GB005349, 2016.

Polovina, J. J., Howell, E. A., and Abecassis, M.: Ocean's least productive waters are expanding, Geophysical Research Letters, 35, 2–6, https://doi.org/10.1029/2007GL031745, 2008.

Possenti, L., Skjelvan, I., Atamanchuk, D., Tengberg, A., Humphreys, M. P., Loucaides, S., Fernand, L., and Kaiser, J.: Norwegian Sea net community production estimated from O_2 and prototype CO_2 optode measurements on a Seaglider, Ocean Science, 17, 593–614, https://doi.org/10.5194/os-17-593-2021, 2021.

Poulin, C., Zhang, X., Yang, P., and Huot, Y.: Diel variations of the attenuation, backscattering and absorption coefficients of four phytoplankton species and comparison with spherical, coated spherical and hexahedral particle optical models, Journal of Quantitative Spectroscopy and Radiative Transfer, 217, 288–304, https://doi.org/10.1016/j.jqsrt.2018.05.035, 2018.

Price, J. F., Weller, R. A., and Pinkel, R.: Diurnal cycling: Observations and Models of the Upper Ocean Response to Diurnal Heating, Cooling, and Wind Mixing, Journal of Geophysical Research, 91, 8411–8427, https://doi.org/10.1029/JC091iC07p08411, 1986.

Qin, C., Guiling, Z., Wenjing, Z., Yu, H., and Sumei, L.: Net community production, nutrients, and hydrographic parameters in the South China Sea in October 2014 and June 2015, https://doi.org/10.5281/zenodo.4496886, 2021a.

Qin, C., Zhang, G., Han, Y., Zhang, G., and Sun, J.: Net community production, nutrients, and hydrographic parameters in the South China Sea in summer 2017, https://doi.org/10.5281/zenodo.6403833, 2021b.

Reuer, M. K., Barnett, B. A., Bender, M. L., Falkowski, P. G., and Hendricks, M. B.: New estimates of Southern Ocean biological production rates from O_2/Ar ratios and the triple isotope composition of O_2, Deep Sea Research I, 54, 951–974, https://doi.org/10.1016/j.dsr.2007.02.007, 2007.

Roemmich, D., Talley, L., Zilberman, N., Osborne, E., Johnson, K., Barbero, L., Bittig, H., Briggs, N., Fassbender, A., Johnson, G., King, B., Mcdonagh, E., Purkey, S., Riser, S., Suga, T., Takeshita, Y., Thierry, V., and Wijffels, S.: The Technological, Scientific, and Sociological Revolution of Global Subsurface Ocean Observing, Oceanography, 2–8, https://doi.org/10.5670/oceanog.2021.supplement.02-02, 2021.

Rosengard, S. Z., Izett, R. W., Burt, W. J., Schuback, N., and Tortell, P. D.: Decoupling of ΔO2/Ar and particulate organic carbon dynamics in nearshore surface ocean waters, Biogeosciences, 17, 3277–3298, https://doi.org/10.5194/bg-17-3277-2020, 2020.

Seguro, I., Marca, A. D., Painting, S. J., Shutler, J. D., Suggett, D. J., and Kaiser, J.: High-resolution net and gross biological production during a Celtic Sea spring bloom, Progress in Oceanography, 177, 101885, https://doi.org/10.1016/j.pocean.2017.12.003, 2019.

Siegel, D. A., Dickey, T. D., Washburn, L., Hamilton, M. K., and Mitchell, B. G.: Optical determination of particulate abundance and production variations in the oligotrophic ocean, Deep Sea Research, 36, 211–222, 1989.

Siegenthaler, U. and Sarmiento, J. L.: Atmospheric carbon dioxide and the ocean, Nature, 365, 119–125, https://doi.org/10.1038/365119a0, 1993.

Slawyk, G., Collos, Y., and Auclair, J.-C.: The use of the 13C and 15N isotopes for the simultaneous measurement of carbon and nitrogen turnover rates in marine phytoplankton1, Limnology and Oceanography, 22, 925–932, https://doi.org/10.4319/lo.1977.22.5.0925, 1977.

Spitzer, W. S. and Jenkins, W. J.: Rates of vertical mixing, gas exchange and new production: Estimates from seasonal gas cycles in the upper ocean near Bermuda, Journal of Marine Research, 47, 169–196, https://doi.org/10.1357/002224089785076370, 1989.

Steeman Nielsen, E.: The Use of Radio-active Carbon (C14) for Measuring Organic Production in the Sea, ICES Journal of Marine Science, 18, 117–140, https://doi.org/10.1093/icesjms/18.2.117, 1952.

Steiner, N., Vagle, S., Denman, K. L., and McNeil, C.: Oxygen and nitrogen cycling in the northeast Pacific - Simulations and observations at Station Papa in 2003/2004, Journal of Marine Research, 65, 441–469, https://doi.org/10.1357/002224007781567658, 2007.

Stoer, A. C. and Fennel, K.: Estimating ocean net primary productivity from daily cycles of carbon biomass measured by profiling floats, Limnology and Oceanography Letters, n/a, https://doi.org/10.1002/lol2.10295, 2022.

Sun, O. M., Jayne, S. R., Polzin, K. L., Rahter, B. A., and Laurent, L. C. S.: Scaling Turbulent Dissipation in the Transition Layer, Journal of Physical Oceanography, 43, 2475–2489, https://doi.org/10.1175/JPO-D-13-057.1, 2013.

Timmerman, A. H. V. and Hamme, R. C.: Consistent Relationships Among Productivity Rate Methods in the NE Subarctic Pacific, Global Biogeochemical Cycles, 35, 1–18, https://doi.org/10.1029/2020GB006721, 2021.

1165   Tortell, P. D.: Dissolved gas measurements in oceanic waters made by membrane inlet mass spectrometry, Limnology and Oceanography: Methods, 3, 24–37, https://doi.org/10.4319/lom.2005.3.24, 2005.

Vagle, S., McNeil, C., and Steiner, N.: Upper ocean bubble measurements from the NE Pacific and estimates of their role in air-sea gas transfer of the weakly soluble gases nitrogen and oxygen, Journal of Geophysical Research, 115, C12054, https://doi.org/10.1029/2009JC005990, 2010.

1170   Volk, T. and Hoffert, M. I.: Ocean Carbon Pumps: Analysis of Relative Strengths and Efficiencies in Ocean-Driven Atmospheric CO_2 Changes, in: The Carbon Cycle and Atmospheric CO_2: Natural Variations Archean to Present, edited by: Sundquist, E. T. and Broecker, W. S., AGU, 99–110, 1985.

Wang, B., Fennel, K., Yu, L., and Gordon, C.: Assessing the value of biogeochemical Argo profiles versus ocean color observations for biogeochemical model optimization in the Gulf of Mexico, Biogeosciences, 17, 4059–4074, 1175   https://doi.org/10.5194/bg-17-4059-2020, 2020a.

Wang, S., Kranz, S. A., Kelly, T. B., Song, H., Stukel, M. R., and Cassar, N.: Lagrangian Studies of Net Community Production: The Effect of Diel and Multiday Nonsteady State Factors and Vertical Fluxes on O2/Ar in a Dynamic Upwelling Region, 0–3 pp., https://doi.org/10.1029/2019JG005569, 2020b.

Wanninkhof, R.: Relationship between wind speed and gas exchange over the ocean revisited, Limnology and Oceanography: 1180   Methods, 12, 351–362, https://doi.org/10.1029/92JC00188, 2014.

Ware, D. M. and Thomson, R. E.: Bottom-Up Ecosystem Trophic Dynamics Determine Fish Production in the Northeast Pacific, Science, 308, 1280–1284, https://doi.org/10.1126/science.1109049, 2005.

Weeding, B. and Trull, T. W.: Hourly oxygen and total gas tension measurements at the Southern Ocean Time Series site reveal winter ventilation and spring net community production, Journal of Geophysical Research: Oceans, 119, 348–358, 1185   https://doi.org/10.1002/2013JC009302, 2014.

Westberry, T., Behrenfeld, M. J., Siegel, D. A., and Boss, E.: Carbon-based primary productivity modeling with vertically resolved photoacclimation, Global Biogeochemical Cycles, 22, https://doi.org/10.1029/2007GB003078, 2008.

Westberry, T. K., Williams, P. J. L. B., and Behrenfeld, M. J.: Global net community production and the putative net heterotrophy of the oligotrophic oceans, Global Biogeochemical Cycles, 26, 1–17, https://doi.org/10.1029/2011GB004094, 1190   2012.

White, A. E., Barone, B., Letelier, R. M., and Karl, D. M.: Productivity diagnosed from the diel cycle of particulate carbon in the North Pacific Subtropical Gyre, Geophysical Research Letters, 44, 3752–3760, https://doi.org/10.1002/2016GL071607, 2017.

Yang, B.: Seasonal Relationship Between Net Primary and Net Community Production in the Subtropical Gyres: Insights 1195   From Satellite and Argo Profiling Float Measurements, Geophysical Research Letters, 48, 1–8, https://doi.org/10.1029/2021GL093837, 2021.

Yang, B., Emerson, S. R., and Bushinsky, S. M.: Annual net community production in the subtropical Pacific Ocean from in-situ oxygen measurements on profiling floats, Global Biogeochemical Cycles, 31, 728–744, https://doi.org/10.1002/2016GB005545, 2017.

1200   Yang, B., Emerson, S. R., and Peña, M. A.: The effect of the 2013-2016 high temperature anomaly in the subarctic Northeast Pacific (the "Blob") on net community production, Biogeosciences, 15, 6747–6759, 2018.

Yang, B., Emerson, S. R., and Quay, P. D.: The Subtropical Ocean's Biological Carbon Pump Determined From O2 and DIC/DI13C Tracers, Geophysical Research Letters, 46, 5361–5368, https://doi.org/10.1029/2018GL081239, 2019.

1205 Yang, B., Fox, J., Behrenfeld, M. J., Boss, E. S., Haëntjens, N., Halsey, K. H., Emerson, S. R., and Doney, S. C.: In Situ Estimates of Net Primary Production in the Western North Atlantic With Argo Profiling Floats, Journal of Geophysical Research: Biogeosciences, 126, 1–16, https://doi.org/10.1029/2020JG006116, 2021.

Yang, B., Emerson, S. R., and Cronin, M. F.: Skin Temperature Correction for Calculations of Air-Sea Oxygen Flux and Annual Net Community Production, Geophysical Research Letters, 49, e2021GL096103, https://doi.org/10.1029/2021GL096103, 2022.

1210